

THESIS

CLAMPING DEVICES TO ENABLE CONCURRENT MECHANICAL AND ELECTRICAL CONNECTIONS
OF A POWER SEMICONDUCTOR

Submitted by

Michael Andrew Shover

Department of Electrical and Computer Engineering

In partial fulfillment of the requirements

For the Degree of Master of Science

Colorado State University

Fort Collins, Colorado

Fall 2011

Master's Committee:

Advisor: George J. Collins

Thomas Wei Chen

Steven C. Reising

Hiroshi Sakurai

Copyright by Michael Andrew Shover 2011

All Rights Reserved

ABSTRACT

CLAMPING DEVICES TO ENABLE CONCURRENT MECHANICAL AND ELECTRICAL CONNECTIONS OF A POWER SEMICONDUCTOR

In response to the restrictions of lead bearing solders in the European Union Restriction of Hazardous Substances Directive of 2002, new strategies for solderless electrical connections are desired. In this work, such concepts are used in the simultaneous electrical connection of power semiconductor leads to a PCBA and mechanical attachment of the device package to a heat sink. These concepts are specifically designed for use in an industrial high power (kW to tens of kW) radio frequency generator. The many constraints of such a system, some of which are directly contradictory to each other, are considered throughout, including manufacturability, mechanical tolerances, system reliability, and cost.

Theoretical models predict that in the expected usage environment, the transistor leads in the clamped connection under consideration will move 5.1 μm for a thermal excursion of 50 °C. SEM micrographs showing that the size of z-axis asperities is on the order of 1 μm and calculations estimating adhesive junctions with surface energies on the order of 100 N/mm^2 demonstrate that contact wear is likely. A survey of available materials has been conducted, with beryllium copper and polyetherimide

being the favored options for clamp construction. Four concepts are modeled, noting the benefits and drawbacks of each.

The preferred embodiment is found to be a clamping mechanism fabricated from electrically insulating material, specifically injection molded 30% fiberglass filled polyetherimide, incorporating cantilevered beams which deflect upon installment into the system with fasteners, thus forming the electrical connections. Test regimens have been performed, including room temperature aging, elevated temperature aging at 50 °C and 80 °C, thermal cycling, highly accelerated life testing, and thermal analysis in both the steady state and transient regimes. The results of the experiments show this clamping system to have a useful life in the intended environment of multiple years.

ACKNOWLEDGEMENTS

The author wishes to acknowledge the groups and individuals who assisted him in producing this work.

First and foremost, I would like to thank my wife Cheryl Refuerzo for her patience and support. My daughter Maya also provided welcomed mental breaks and a regular reminder of what is truly important.

I would like to thank my advisor George Collins, for impetus, guidance, and encouragement.

I would also like to thank Advanced Energy Industries for providing a research oriented and challenging workplace at which works such as this can be conceived and developed.

DEDICATION

This work is dedicated to my parents, James and Janice, who instilled in me at a very early age the importance of an inquisitive nature and a good education. For this, I am forever grateful.

TABLE OF CONTENTS

ABSTRACT	ii
ACKNOWLEDGEMENTS	iv
DEDICATION	v
LIST OF FIGURES	viii
CHAPTER 1 - INTRODUCTION	1
1.1 Description of project	1
1.2 Organization of thesis	2
CHAPTER 2 - REQUIREMENTS AND CONSTRAINTS	4
2.1 RoHS-compliant solder	4
2.2 Design for manufacturability	6
2.3 Downforce on device package	8
2.4 Downforce on device leads	9
2.5 Useful life	11
2.6 Electromagnetic heating	12
2.7 Electrical insulation	13
2.8 Accommodation of mechanical tolerances	14
2.9 Cooling of device die	16
CHAPTER 3 - INTERACTION OF DEVICE LEAD AND PRINTED CIRCUIT BOARD	24
3.1 Movement of device lead	24
3.2 Asperities	31
3.3 Contact wear	36
3.4 Corrosion	43
CHAPTER 4 - ANALYSIS OF AVAILABLE MATERIALS	45
4.1 - Polyphenylene sulfide	45

4.2 – Polyetherimide.....	46
4.3 – Spring steel.....	47
4.4 – Beryllium copper.....	47
4.5 – Polypropylene	48
CHAPTER 5 - CONCEPTS FOR ATTACHMENT.....	49
5.1 – Single lead	49
5.2 – Metal frame, insulating tabs.....	51
5.3 – Metal frame, insulating sheet.....	53
5.4 – Insulating frame	55
CHAPTER 6 - EXPERIMENTAL RESULTS AND DISCUSSIONS	58
6.1 – Room temperature relaxation	59
6.2 – Thermal cycling	62
6.3 – Elevated temperature relaxation.....	65
6.4 – Highly Accelerated Life Test.....	71
6.5 – Steady state and transient thermal testing	73
CHAPTER 7 - CONCLUSIONS AND FUTURE WORK	82
REFERENCES	85

LIST OF FIGURES

Figure 2.1 – Kyocera M177 package.	6
Figure 2.2 – Microsemi T11 package.	6
Figure 2.3 – Relationship between number of process steps and yield.....	8
Figure 2.4 – Simplified schematic of an RF amplifier showing additional contact resistance.	11
Figure 2.5 – Electrical path length for automated IR reflow of solder paste.	12
Figure 2.6 – Electrical path length for solder-free connections.	13
Figure 2.7 – Total Z-dimension stackup when assembly tolerances are at minimum.	16
Figure 2.8 – Total Z-dimension stackup when assembly tolerances are at maximum.....	16
Figure 2.9 – Thermal model of VHF MOSFET, heat spreader, and heat sink.	18
Figure 2.10 – Mean Time to Failure vs Temperature, SD2933.	20
Figure 2.11 – Lumped capacitance model for MOSFET / heat sink system.	23
Figure 3.1 – Kyocera M177 package and PCB.....	27
Figure 3.2 – Representative materials used in a VHF MOSFET.	28
Figure 3.3 – System movement under thermal cycling leading to lead flexure.....	30
Figure 3.4 – System movement under thermal cycling leading to lead movement.	31
Figure 3.5 – Levels of asperity.	33
Figure 3.6 - Initial contact of two spherical asperities.....	33
Figure 3.7 - Compression contact of two spherical asperities.....	34
Figure 3.8 – SEM micrograph of VHF MOSFET lead surface.	37
Figure 3.9 – SEM micrograph of gold plated PCB trace.....	37
Figure 3.10 – Domains of contact wear.	38
Figure 3.11 – Two-body abrasion mechanisms.	41
Figure 3.12 – Three-body abrasion mechanisms.....	41

Figure 3.13 – Crack formation in sliding surface fatigue.	44
Figure 5.1 – Isometric view of clamp for single transistor lead.....	51
Figure 5.2 – Four single-lead clamps in the system.....	51
Figure 5.3 – Metal clamp with insulating tabs.....	53
Figure 5.4 – Metal clamp with insulating tabs in the system.	53
Figure 5.5 – Insulating sheet and metal frame clamp components.....	55
Figure 5.6 – Metal frame clamp and insulating sheet in the system.	55
Figure 5.7 – Insulating clamp.	58
Figure 5.8 – Insulating clamp in the system.	58
Figure 6.1 – Room temperature relaxation of beryllium copper with polypropylene insulating sheet.	62
Figure 6.2 – Room temperature relaxation of Ultem clamp.	63
Figure 6.3 – Thermal cycling profile and chamber response.....	64
Figure 6.4 – Relaxation behavior of Ultem clamp during thermal excursions.	65
Figure 6.5 – Relaxation trend of Ultem clamp during thermal cycling, reduced data.	66
Figure 6.6 – Relaxation of beryllium copper clamping system at 50 °C.	68
Figure 6.7 - Relaxation of Ultem clamp at 50 °C.....	69
Figure 6.8 - Relaxation of Ultem clamp at 80 °C.....	70
Figure 6.9 – Acceleration factor vs. temperature for Ultem clamps.....	71
Figure 6.10 - Graphical depictions of the five HALT segments.....	73
Figure 6.11 – Ultem clamp and decapsulated VHF MOSFET.	75
Figure 6.12 – VHF MOSFET with identifying annotation.	76
Figure 6.13 – Measured temperatures of the device die and clamping mechanism.....	77
Figure 6.14 – Thermal images of the device die and clamping mechanism.....	79
Figure 6.15 – Temperature rate of change of VHF MOSFET dice.	80
Figure 6.16 – Temperature rate of change of MOSFET leads and exposed bulk package.	81

CHAPTER 1 - INTRODUCTION

1.1 Description of project

Over the past decade, the interest in environmental responsibility and sustainability has increased in accordance with the publications of scientific literature detailing the hazards of long-term, low-level exposure to specific materials. Simultaneously, the globally increasing middle-class demographic has led to a dramatic increase in the annual quantity of electronic waste, as a larger percentage of the world population regularly upgrades their mobile phones, microwaves, laptop computers, and similar nondurable goods. To address this growing problem, in 2002 the European Union (EU) took under consideration six substances which were commonly used in the production of electronics, all of which are known or suspected carcinogens or neurotoxins: lead, mercury, cadmium, hexavalent chromium, polybrominated biphenyls (PBBs), and polybrominated diphenyl ether (PBDE). In an effort to limit the disposal and eventual diffusion of these substances into the environment, the EU ratified the Restriction of Hazardous Substances (RoHS) Directive 2002/95/EC on 27 January 2003 [1].

Some exemptions from the RoHS Directive are in place, such as those for implantable medical devices and large scale industrial tools. The EU is currently evaluating these exemptions, and may take a number of actions, including adding

additional substances to the 'banned' list, weakening the language used for the exemptions, or both [2]. Manufacturers of currently exempted equipment are now faced with the challenge of removing these harmful substances from their products, most notably tin-lead eutectic (63% Sn, 37% Pb) solder. This standard solder has been well characterized in the electronics industry for decades. Studies have shown that in some applications, long-term reliability concerns exist with using RoHS-compliant solder [3-8]. These concerns are compounded when relatively high voltages, currents, and frequencies are involved, driving manufacturers to eliminate solder for these types of connections. The electrical connections from electronic parts to printed circuit board assemblies (PCBAs) still must exist, so alternate strategies are required if soldering the joints is not desired.

1.2 Organization of thesis

This thesis explores such concepts for use with power semiconductors specifically in an industrial high power radio frequency generator. Chapter 2 describes the rationale for avoiding RoHS-compliant solders and the detailed requirements and constraints of solder-free concepts. In Chapter 3, theory and discussion are introduced regarding the construction of a connector from a semiconductor lead and a PCB pad, and data from relevant experimentation is presented. Chapter 4 looks into the materials which are available for mechanical attachment. Chapter 5 introduces four concepts in which a single mechanical clamping device is used to simultaneously electrically connect a power semiconductor to a PCBA and mechanically attach the

device package to a heat sink; two concepts are developed further and prototyped. Chapter 6 presents the results of experimentation of the two concepts, and a preferred design is selected, the choice based on multiple parameters. Chapter 7 summarizes the current work and speculates on potential future work on this topic.

CHAPTER 2 - REQUIREMENTS AND CONSTRAINTS

2.1 RoHS-compliant solder

There are numerous types of solders which do not contain any of the banned substances in the RoHS directive. Most are variants of Sn-Ag-Cu, commonly known by its acronym 'SAC.' The most common alloy, SAC305 (Sn96.5Ag3.0Cu0.5) has a melting temperature of 217 °C, a 30 °C increase over the melting temperature of Sn63Pb37 at 187 °C. Good results are clearly possible when automated processes, such as wave and infrared reflow are possible [9]. Certain types of power semiconductors, however, do not lend themselves to wave or oven reflow, such as the M177 package developed by Kyocera and the T11 package developed by Microsemi, shown respectively in Figure 2.1 and Figure 2.2. Packages such as these are designed specifically for VHF and UHF power amplification and can dissipate over 800 watts when adequate cooling is supplied. Metal screws are typically used to secure the package to a heat sink and then the leads are manually soldered to the PCBA. Products designed for broadcast, military, and industrial applications commonly use RF power levels on the order of kilowatts or even tens of kilowatts, requiring a large number of these devices. Even with Sn63Pb37 solder, which has excellent wetting and workability characteristics, the opportunities for eventual device failure due to poor workmanship are significant, given the sheer quantity of joints to be soldered. The process to manufacture high reliability products

will often require an inspection of all manual solder joints by a second assembler, increasing the total time required for soldering the device leads to multiple hours. This of course has the secondary effect of adding cost to the final product, which may not be easily quantified unless a 'total cost' model is used [10]. Because a human is involved in the process, the repeatability from joint to joint is inherently low.

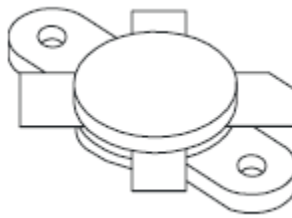


Figure 2.1 – Kyocera M177 package.

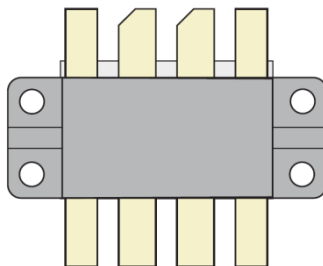


Figure 2.2 – Microsemi T11 package.

Manual soldering with Pb-free solder introduces considerably more difficulties. The wetting and workability characteristics are noticeably inferior, requiring assemblers with more advanced skills to manually solder parts. The device leads and the PCBA pads must be heated the additional 30 °C, which increases the likelihood of damage to the

device and the PCB laminate. While solder joints made with Sn63Pb37 can be easily inspected for quality, those made with Pb-free solder pose more problems [11]. The problems introduced by gold embrittlement and growth of intermetallic compounds, which weaken the solder joint, are a concern for high-frequency devices, as the leads are often gold plated [12, 13]. Fatigue properties of Pb-free solders are variable when compared to Sn63Pb37; the thermal excursions that the solder joint experiences dictate which type of solder will exhibit more thermal cycles before failure [14], [15]. In the event that the device and/or PCBA needs to be reworked or repaired, the addition of corrosive organic flux can be necessary to achieve the necessary level of Pb-free solder removal [16]. Automated soldering with Pb-free solder is an option which addresses the areas of repeatability and workmanship, but the other issues remain. Furthermore, laser reflow, hot thermode, or hot air selective soldering processes add cost to the product; a contract electronics manufacturer will charge extra for the process time and equipment usage, and if performed in house, significant capital equipment expenditure is required.

2.2 Design for manufacturability

Designing a product for the manufacturing environment involves numerous considerations, including part design and tolerances, human factors and motions, order of assembly operations, and serviceability. It is in the company's best interest to design products which can be manufactured in as few steps as possible. The number of process steps per assembly phase and its effect on overall product yield is illustrated in

Figure 2.3 –; note that sigma represents one standard deviation from the process mean [17]. A manufacturing process which is reasonably matured at the $\pm 5\sigma$ but not fully optimized to the $\pm 6\sigma$ level can realize a yield improvement of 0.47% by reducing the number of steps from 60 to 40. This may seem trivial, but if there are twenty such processes which are involved in the construction of the full product, the total yield increases from 76% to 83%, a 9.8% improvement. This has quantifiable benefits for order delivery times, assembly and test equipment efficiencies, manufacturing line throughput, and total product cost.

Overall Yield in Percent vs. Sigma				
<i>(distribution shifted 1.5σ to account for process deviations)</i>				
# of Parts or Steps	$\pm 3\sigma$	$\pm 4\sigma$	$\pm 5\sigma$	$\pm 6\sigma$
1	93.32	99.379	99.9767	99.99966
7	61.63	95.733	99.839	99.9976
10	50.08	93.96	99.768	99.9966
20	25.08	88.29	99.536	99.9932
40	6.29	77.94	99.074	99.9864
60	1.58	68.81	98.614	99.9796
80	0.40	60.75	98.156	99.9728
100	0.10	53.64	97.70	99.966
150	----	39.38	96.61	99.949
200	----	28.77	95.45	99.932
300	----	15.43	93.26	99.898
400	----	8.28	91.11	99.864
500	----	4.44	89.02	99.83

Figure 2.3 – Relationship between number of process steps and yield.

Maximizing repeatability is another aspect of designing for manufacturability. A highly repeatable process is statistically more likely to deliver products which meet specification than a process which is uncontrolled [18]. In a traditional operation, a device is first secured to the heat sink with two to four screws. The leads are then manually soldered, requiring at the very least four steps which vary based on operator skill, and a total of six to eight steps per device. A clamping mechanism which provides the necessary mechanical and electrical connections could theoretically be held in place by two screws. This reduces the number of steps by a factor of two or three, and removes all variability if calibrated torque-stop hardware is used. With respect to manufacturability, the benefit of a clamping mechanism can clearly be quite substantial.

2.3 Downforce on device package

To maintain a desired cooling rate, the device package must be secured to the heat sink with a certain amount of force. The packages in Figure 2.1 and Figure 2.2 have screw holes to facilitate this attachment. For a specific screw and surface area, the maximum achievable pressure can be calculated. The constraints are: (1) the maximum torque the screw can withstand before the screw head shears from the threaded portion of the screw body, and (2) the maximum force exerted by the screw threads which the heat sink can withstand before deforming. The package is commonly made of brass, copper, or another metal, and can easily withstand pressures in the MPa range. Naturally, a clamping mechanism must meet the same criteria. This constraint is easily

satisfied, as most clamping mechanisms will use the device screw holes as part of the attachment strategy.

2.4 Downforce on device leads

When the semiconductor device leads are soldered, the solder provides the electrical connection between the leads and the PCBA. When the leads are mechanically clamped to the PCBA, there will be a minimum force which the clamping mechanism must exert to maintain the maximum tolerable contact resistance.

There are at least two aspects of contact resistance which determine how much resistance is allowable. The first consideration is the direct effect on circuit performance that is introduced by the contact resistance. In a simple FET amplifier, resistances in the gate, drain, and source leads have individual sensitivities which will be circuit dependent. An RF MOSFET amplifier, as shown in Figure 2.4, is generally most sensitive to the added resistance in the drain lead, as this will lower the maximum output voltage of the amplifier.

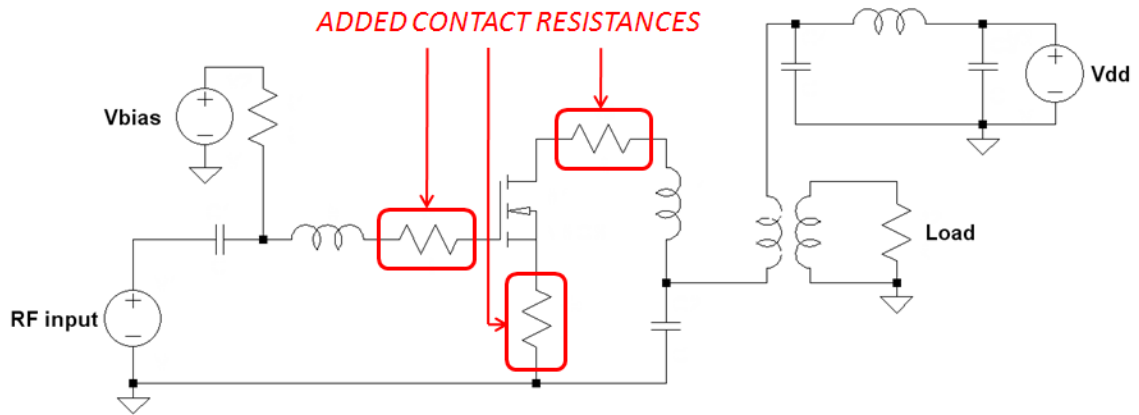


Figure 2.4 – Simplified schematic of an RF amplifier showing additional contact resistance.

Another consideration is the resistive heating of the contact. These are I^2R losses which can be easily calculated using Equation (2.1),

$$P = I^2 \cdot \frac{\rho \cdot l}{a} \quad (2.1)$$

where $P = \text{power (W)}$

$I = \text{current (A)}$

$\rho = \text{resistivity } (\Omega \cdot \text{m})$

$l = \text{electrical path length (m)}$

$a = \text{contact area (m}^2\text{)}$

The path length for a typical solder connection which has been made via infrared reflow of eutectic solder paste, as illustrated in Figure 2.5, is approximately 0.5 mm. For solder-free connections, the comparable path length is only on the order of 0.05 mm,

even in the case of significant surface irregularities and asperities, as illustrated in Figure 2.6. As most high-frequency power devices have gold-plated leads, the solder-free connection has a lower contact resistance and hence less resistive heating.

2.5 Useful life

The customers for industrial electronics, such as those which use the high-frequency power devices previously discussed, expect the capital equipment they invest in to have a reasonably long life. Ten years of nearly continuous usage with no planned preventive maintenance is a requirement in certain markets, such as the semiconductor fabrication industry. This is a difficult constraint for power electronics, although not unattainable.

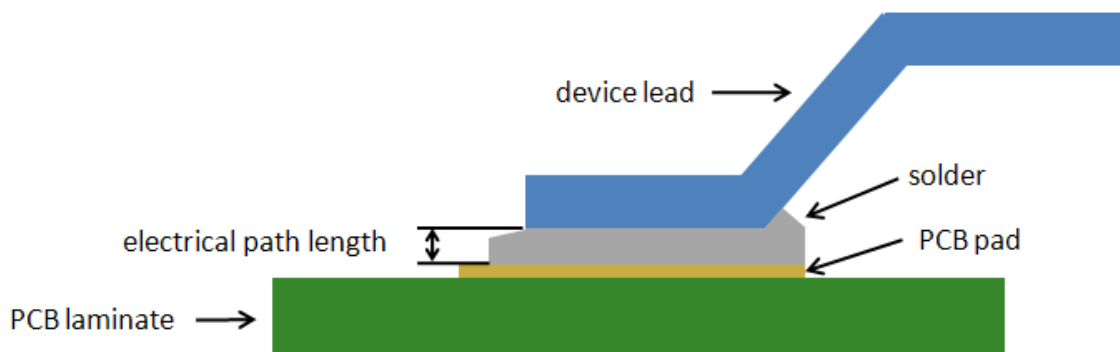


Figure 2.5 – Electrical path length for automated IR reflow of solder paste.

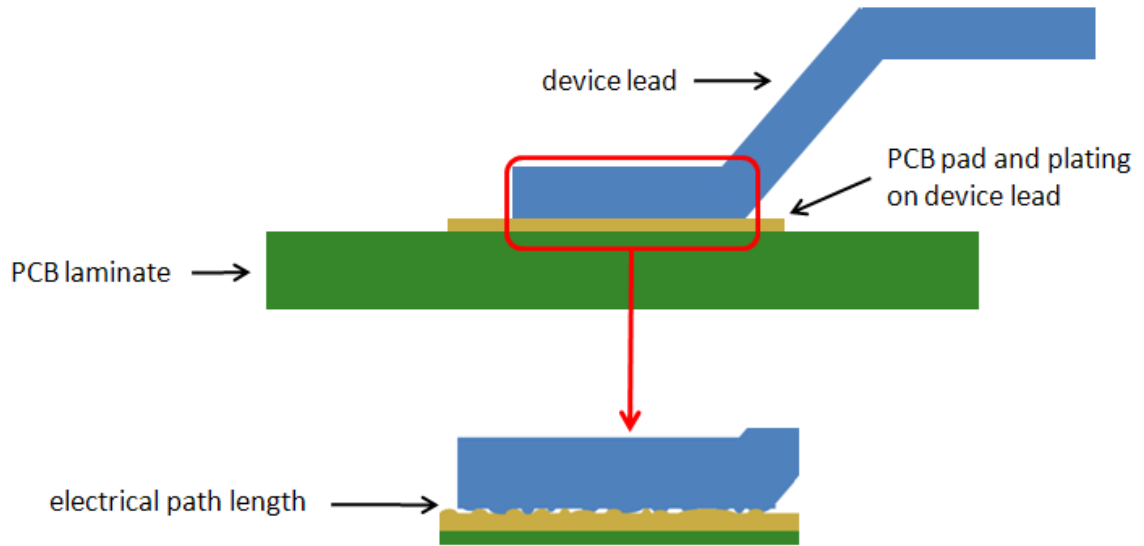


Figure 2.6 – Electrical path length for solder-free connections.

Solder, whether Sn63Pb37 or Pb-free, has a long and well characterized useful life. When the connection is mechanically clamped, different factors come into play. The member exerting the force on the device leads may be susceptible to fatigue, relaxation, and embrittlement. Each of these degradation mechanisms is likely to be nonlinear with respect to both time and applied temperature, and depending on the material used, may not be well characterized in a long-term application. The required useful life determines, in a large way, suitability of a given material for mechanical clamping of the device leads, especially when lifetimes on the order of ten years or more are needed.

2.6 Electromagnetic heating

Any clamping mechanism must be minimally susceptible to all types of electrically induced heating. Insulating materials can experience dielectric heating. Polar molecules align themselves in an electromagnetic field; if the field is time-varying, the molecules continue to move, creating collisions with adjacent molecules and releasing energy in the form of heat [19]. This type of heating is generally not an issue with metals, however this factor needs to be considered for a clamp made from an electrically insulating material. Furthermore, different types and grades of high-performance engineering polymers have different levels of sensitivity to dielectric heating; the performance of lower grade plastics is even less favorable.

2.7 Electrical insulation

The power semiconductor devices under consideration have multiple electrical connections. In a MOSFET, there are three, namely the gate, drain, and source. All practical circuits using these devices require a minimum amount of electrical resistance between these connections. The actual minimum resistance required will be dependent on factors such as circuit topology and desired performance, but resistance values on the order of megohms are generally acceptable.

This constraint precludes a simple and inexpensive clamping solution such as a part made from a single stamped piece of spring steel, which would introduce a very low resistance path between the device leads. An electrically insulating material must

be employed to some degree, if not exclusively. Many acceptable materials are available such as polymers and fiber-reinforced phenolic and epoxy resins.

2.8 Accommodation of mechanical tolerances

In an assembly comprised of a semiconductor device, heat sink, PCBA, and associated mounting hardware such as screws, there are mechanical tolerances which are specified for each part. These tolerances are to account for the normal variation of typical production processes. When the semiconductor device leads are soldered to the PCBA, the leads are physically held in place during soldering. After the solder solidifies, the leads remain attached to the PCBA and, unless all parts in the assembly are at their nominal measurements, a permanent deformation of the lead now exists. The device lead has effectively absorbed the mechanical tolerances of the part variations.

If a mechanical clamping device is to be used, the member exerting the downforce on the device leads must be capable of producing and maintaining the required downforce for all possible combinations of dimensional tolerances. Referring to Figure 2.7 and Figure 2.8, the PCB laminate, PCB pad and the device lead have thickness tolerances; the geometry of the device lead has angular tolerances; the heat sink to which the device is attached (not shown) has thickness and flatness tolerances. Most power semiconductors generate a fair amount of heat, so the thermal expansion and contraction of these parts adds another level of complexity to the physical tolerance requirements. A clamping mechanism needs to accommodate all of these tolerances and ensure that: (1) when the total mechanical dimensions are at a minimum as in

Figure 2.7, the downforce is sufficiently high and, (2) similarly ensuring that when the dimensions are at a maximum as in Figure 2.8, the downforce is not so high that it results in compression damage to any part of the assembly.

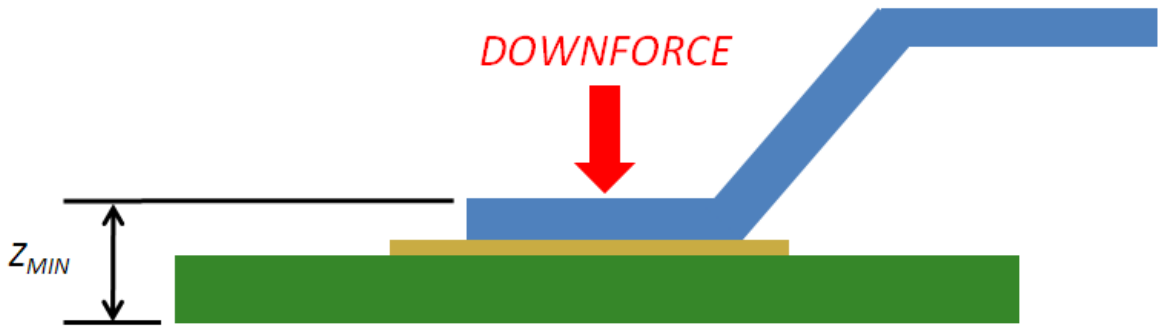


Figure 2.7 – Total Z-dimension stackup when assembly tolerances are at minimum.

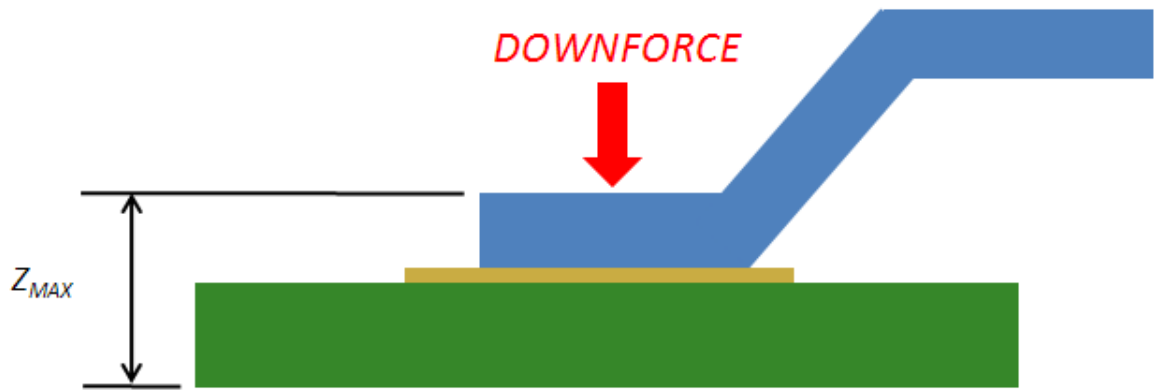


Figure 2.8 – Total Z-dimension stackup when assembly tolerances are at maximum.

2.9 Cooling of device die

The negative effects of high temperatures on a power semiconductor are widely published in textbooks and industry literature. Maintaining a steady state temperature that is well within the bounds of what the specific device can reliably tolerate is a requirement, which if ignored leads to premature failures. Transient temperatures, such as those which the device is exposed to as power is applied, are also of importance because they can cause latent failures on a longer time scale.

Any clamping mechanism devised should at a minimum maintain the same steady state and transient thermal dissipation characteristics as those in an assembly which is soldered. As heat is mainly transferred from the die to the heat sink through a baseplate, as in Figure 2.1 and Figure 2.2, the clamping mechanism is required to maintain a minimum pressure on the baseplate with threaded fasteners attaching the baseplate to the heat sink. A smaller portion of the generate heat is dissipated through the device leads, almost exclusively the drain and source leads in a MOSFET. The downforce provided by the clamping mechanism onto the device leads must be high enough not to compromise this additional thermal path. The thermal model of the device and heat sink system is illustrated in Figure 2.9.

Removing heat from the device die is achieved through conduction, which involves activity at the molecular level; the transfer of heat energy moves from more energetic to less energetic particles via physical interaction between particles. Fourier's law is the basic governing rate equation which describes conduction:

$$q'' = -k\Delta T = -k \left(i \frac{\partial T}{\partial x} + j \frac{\partial T}{\partial y} + k \frac{\partial T}{\partial z} \right) \quad (2.2)$$

where q'' = heat flux vector (W/m^2)

k = thermal conductivity ($W/m \cdot K$)

T = temperature ($^{\circ}K$).

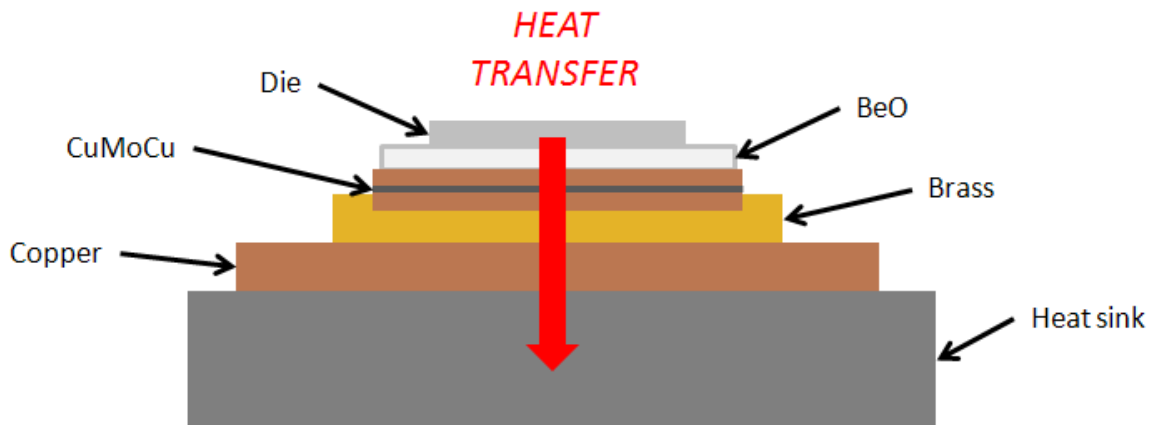


Figure 2.9 – Thermal model of VHF MOSFET, heat spreader, and heat sink.

The heat flux is the rate of heat transfer per unit area, and is proportional to the temperature gradient. It follows that for a given device die temperature, the heat flux will increase as the temperature of the heat sink is lowered, which is desirable. The thermal conductivity is an inherent material property and is relevant to ensure that only materials which are to heat transfer are used in constructing the thermal system. Thermal diffusivity is of interest in the transient domain, and describes the ability of a material to conduct thermal energy relative to its ability to store thermal energy, and is expressed as

$$\alpha = \frac{k}{\rho c_p} \quad (2.3)$$

where α = thermal diffusivity (m^2/s)

ρ = density (kg/m^3)

c_p = specific heat ($J/kg \cdot K$).

Materials with a higher thermal diffusivity value respond faster to induced changes in the thermal environment than those with lower value. A summary of the thermal conductivities and diffusivities for the materials in a thermal system comprised of a VHF MOSFET and heat sink are tabulated in Table 2.1.

Table 2.1 – Thermal Conductivities and Diffusivities

Material	Thermal Conductivity (W/m · K)	Thermal Diffusivity (m²/s)
Beryllium oxide	265	7.5×10^{-5}
Copper-Molybdenum-Copper	170	7.2×10^{-5}
Brass	119	3.4×10^{-5}
Copper	401	1.1×10^{-4}
Aluminum	237	8.4×10^{-5}

The VHF MOSFET being used in the system, an ST Microelectronics SD2933 or Microsemi Corporation VRF2933 can be operated with a maximum die temperature of

200 °C, which is high for a silicon-based semiconductor. There are however reliability implications of operating the device at or near this temperature; the Mean Time to Failure (MTTF) of the device decreases as the die temperature increases. Empirical MTTF data from ST Microelectronics shows this trend, which is illustrated in Figure 2.10. If the device is operated with a die temperature of 100 °C as opposed to 200 °C, the expected reliability gain is a factor of 548 times, which is clearly enormous. When multiple devices are used in the same final product, the reliability gains or penalties are amplified, as the opportunities for failure of any given device is linearly correlated to the total number of devices used.

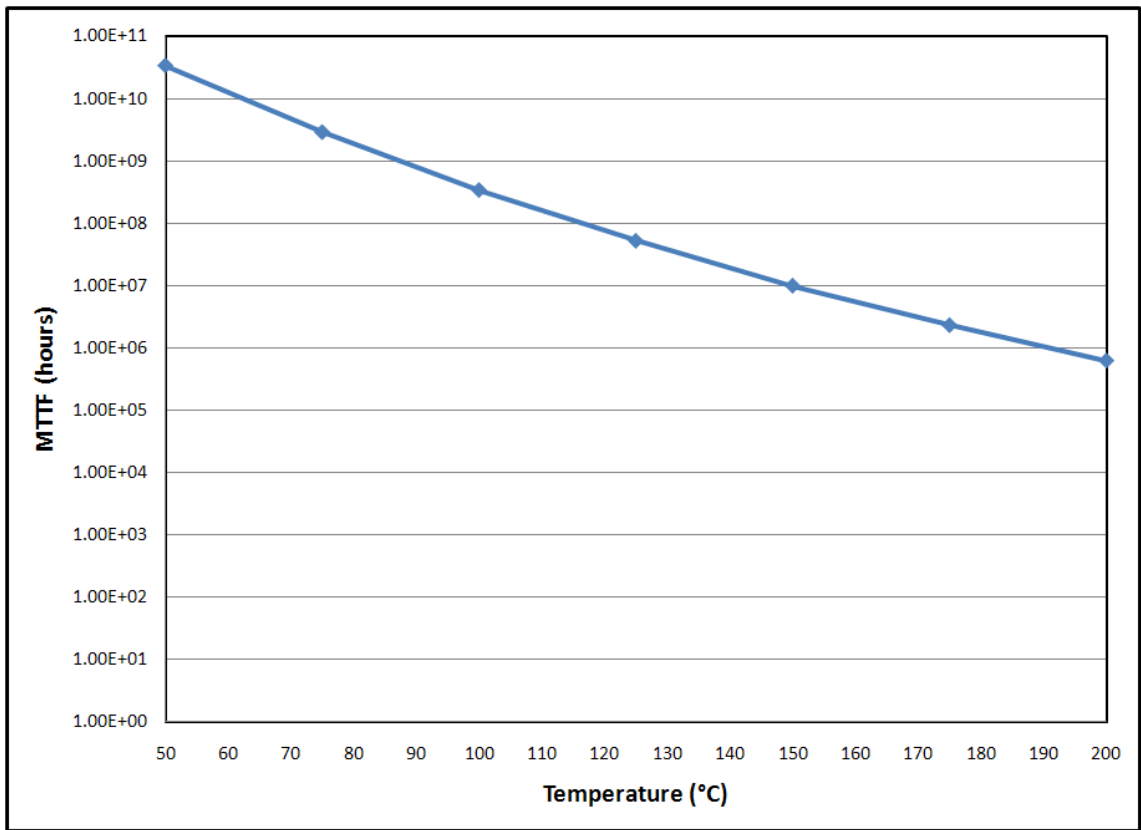


Figure 2.10 – Mean Time to Failure vs Temperature, SD2933.

In a typical application, the output of the VHF MOSFET is on the order of 150 to 350 W of RF power, where the efficiency ranges from 40 to 70%, depending on the bias point and the operational mode of the amplifier. This leaves 100 to 225 W per device to dissipate into the heat sink. If a die temperature of no more than 150 °C is desired under the worst steady state conditions, such as a mismatched static load or a plasma during ignition, a total thermal resistance for each device in the product must be no greater than 0.58 °C/W.

The lumped capacitance method is the prevailing technique for calculating conductance in the transient domain. The initial step involves calculation of the Biot number, a dimensionless parameter which relates the thermal impedances in the bulk of and at the surface of a body, given by

$$Bi = \frac{hL}{k} \quad (2.4)$$

where h = heat transfer coefficient ($\text{W}/\text{m}^2 \cdot \text{K}$)

L = characteristic length (m).

A Biot number of less than one signifies a problem of decreased complexity, as isothermal temperature fields can be assumed. Furthermore, systems with Biot numbers of less than 0.1 can make use of the lumped capacitance method with very low error.

The thermal time constant is the other parameter which is necessary for a transient analysis with the lumped capacitance method; it is expressed by

$$\tau_t = \frac{1}{hA_S} (\rho V_C) \quad (2.5)$$

where τ_t = thermal time constant (s)

A_S = surface area (m^2)

V_C = volume (m^3).

Like its analog in electrical circuits, this quantity expresses the time in which an exponentially decaying quantity reaches $1/e$ times its original value and hence provides an estimation in the transient domain of how quickly a system or parts of a system change temperature.

The lumped capacitance model for the thermal system of Figure 2.9 is shown in Figure 2.11. The Biot numbers for the system under analysis are all lower than 0.1, indicating thermally 'thin' bodies, and showing that the lumped capacitance model is applicable. At a hypothetical time $t=0$, the switch is closed, and the dissipated power flows from the source into the bodies which comprise the system. Each body is represented as a parallel RC circuit with an different time constant. Power eventually flows into the heat sink, which for the purposes of this work is constrained only by its heat transfer coefficient, which is assumed to be constant over the temperatures of interest.

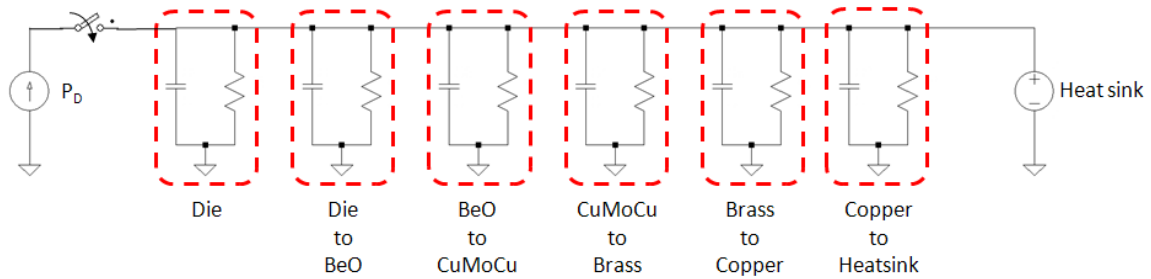


Figure 2.11 – Lumped capacitance model for MOSFET / heat sink system.

Using Equation (2.5) the time constants for the system are calculated; the results are shown in Table 2.2. The calculated time constants are estimations, as previously calculated data for similar heat sinks was used for the heat transfer coefficient, and the areas and volumes of the MOSFET internals are proprietary information; these figures were estimated using measurements obtained with an optical comparator. The time constants are reasonable, given published data regarding comparative thermal conductivities, densities, and thermal diffusivities. The transient cooling of the system will be dominated by the brass body, as the time constant is the largest. It is also noteworthy that if the product is to be used in an application which cycles RF power on and off at a rate which is less than two seconds, fatigue due to thermal cycling may be limited; only cycling which allows the die to cool for two to three seconds would likely induce such failure mechanisms.

Table 2.2 – Calculated thermal time constants.

<i>Body</i>	<i>Thermal time constant (ms)</i>
Beryllium Oxide	450
Copper-Molybdenum-Copper	10
Brass	980
Copper	120

CHAPTER 3 - INTERACTION OF DEVICE LEAD AND PRINTED CIRCUIT BOARD

When the electrical connections between the semiconductor device leads and the PCBA pads are soldered, the interface of a lead with a corresponding pad comprises a small but well defined system. As with all systems, there are constraints which present design and manufacturability challenges. The device lead is likely gold plated, which when soldered creates intermetallic compounds, weakening the solder joint.

When the device lead is mechanically clamped to the PCBA, the interface system changes considerably. Solder and the concern over intermetallic compounds are no longer present. Other mechanisms which warrant attention arise, and are explained, along with analysis regarding the severity and likely impact on a typical clamped connection.

3.1 Movement of device lead

The elasticity of the semiconductor device leads is a factor which needs to be considered for high reliability products. When a high power semiconductor is dissipating a large amount of power, the die heats up, along with the rest of the package.

The coefficient of thermal expansion (CTE) describes how the physical size of a material changes with a change in temperature. Materials with a high CTE expand with increasing heat and contract with decreasing heat. This is a parameter of particular

interest in designing power semiconductor devices and equipment due to the large temperature variations which can occur during normal operation. Power electronic parts and assemblies which are physically constrained in at least one dimension must be designed of materials exhibiting similar CTEs to avoid material fatigue and eventual device failure due to progressive degradation of the material.

The lead material of the power semiconductor can be comprised of a wide array of metals. Tinned copper alloy leads are the most common, as they present a good compromise between performance and cost. RF power semiconductors typically employ a different strategy. Devices using the Kyocera M177 package, such as the SD29xx series by SD Microelectronics [20] and the VRFxxx series by Microsemi Corporation [21], utilize Kovar, a steel alloy, as the base metal for the leads for two main reasons. First, the usage of any steel alloy will increase the physical robustness of a device which is used primarily by high-reliability products. Second, Kovar has been chosen specifically for its low CTE of 4.5 ppm/°C, making it a very low expansion alloy [22], minimizing the effects of many thermal excursions during the expected product lifetime. The Kovar is then plated with nickel, which provides wear resistance, as will be explored later. The final plating is gold, to account for the skin effect, which is significant at high frequencies. The Kovar base metal is 5 mils thick, while the nickel and gold are 0.1 mil and 0.05 mil thick respectively. The mechanical properties of the Kovar base metal, representing approximately 94% of the total cross sectional thickness, will dominate the behavior of the lead and render the physical effects of the nickel and gold platings insignificant with respect to lead elasticity.

The Kyocera M177 package and a representative PCB are shown in Figure 3.1. The MOSFET has a body which is constructed of brass and a ceramic protective cap covering the die. The PCB material may be the commonly used FR-4, a woven fiberglass cloth with an epoxy resin binder, or a more exotic high frequency material such as a ceramic or polytetrafluoroethylene (PTFE).

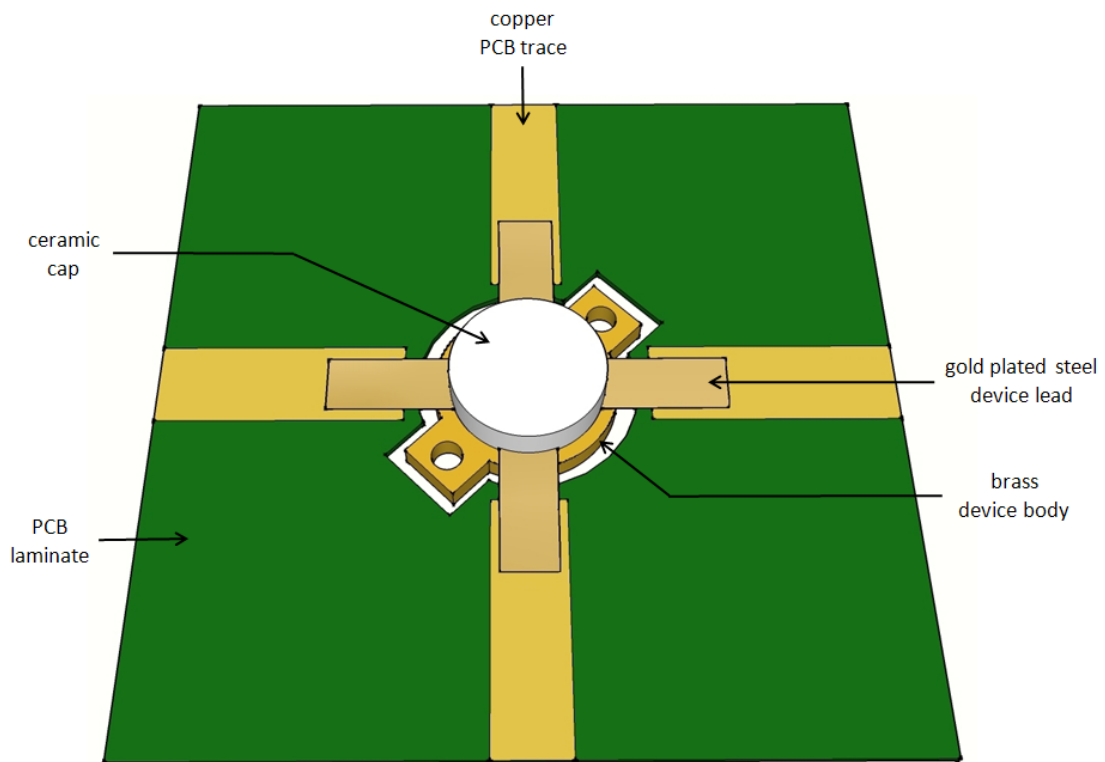


Figure 3.1 – Kyocera M177 package and PCB.

As illustrated in Figure 3.2, the internal view of a VHF MOSFET is constructed of materials which have similar CTEs, which are tabulated in Table 3.1. The beryllium oxide (BeO) layer provides high thermal conductivity from the die to the heat sink while maintaining electrical isolation; these two simultaneous requirements rule out all other practical materials. The copper-molybdenum-copper slug between the brass body and the BeO layer serves to provide CTE matching / isolation.

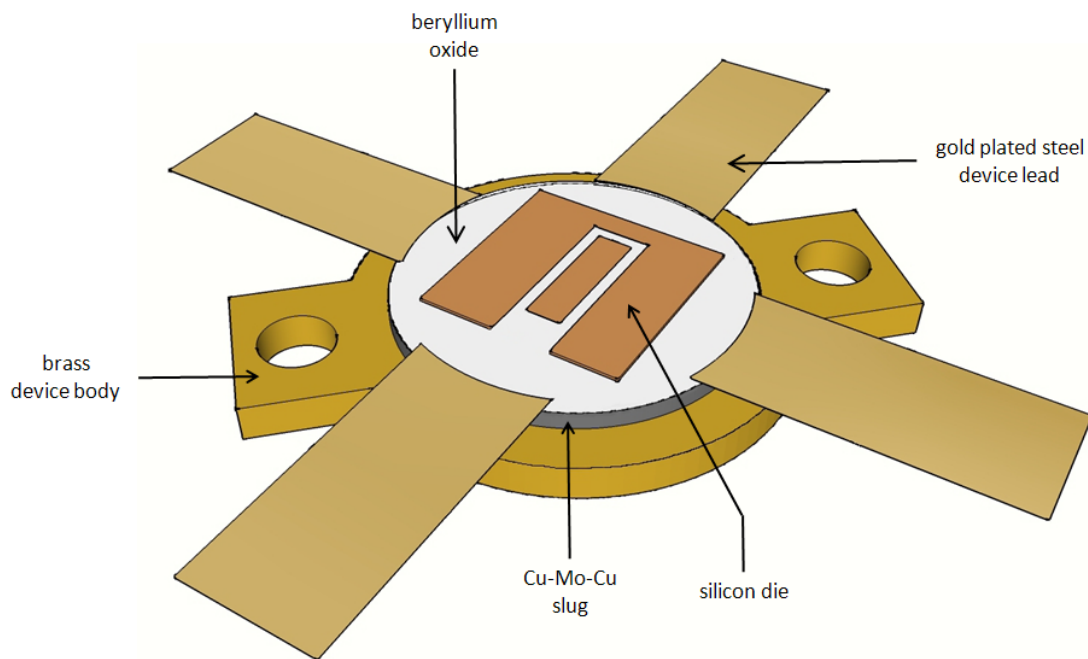


Figure 3.2 – Representative materials used in a VHF MOSFET.

Table 3.1 – CTEs for materials used in high frequency PCBA layout.

<i>Part</i>	<i>Material</i>	<i>CTE (x, y, z; ppm / °C)</i>
PCB laminate (standard)	FR-4	15, 15, 80
PCB laminate (alternate)	Rogers 3210	13, 13, 34
PCB metal layers	Copper	17.6
Transistor body	Brass	19
Transistor base	Copper-Molybdenum-Copper	5.8
Transistor thermal interface	Beryllium oxide	6.6
Transistor leads	Kovar	4.5
Transistor die	Silicon	3

Even with all the considerations for usage of low-CTE materials of the device and PCB, there are movements associated with the application and removal of electrical power to the device, particularly when the device is dissipating hundreds of watts. All of the materials will expand when power is applied and the system heats up; the materials will then contract when power is removed and the system cools. For a mechanically clamped electrical connection, the downforce provided by the clamping mechanism could be large enough to constrain the lead movement with respect to the PCB and cause lead flexure, as illustrated in Figure 3.3. This would require pressures high enough to be unrealistic from a practical clamp. It also introduces a constraint boundary at the point where the device lead meets the package. As the Kovar leads are relatively stiff,

there will be accumulated fatigue damage at this interface, resulting in delamination of the lead from the BeO layer and eventual device failure.

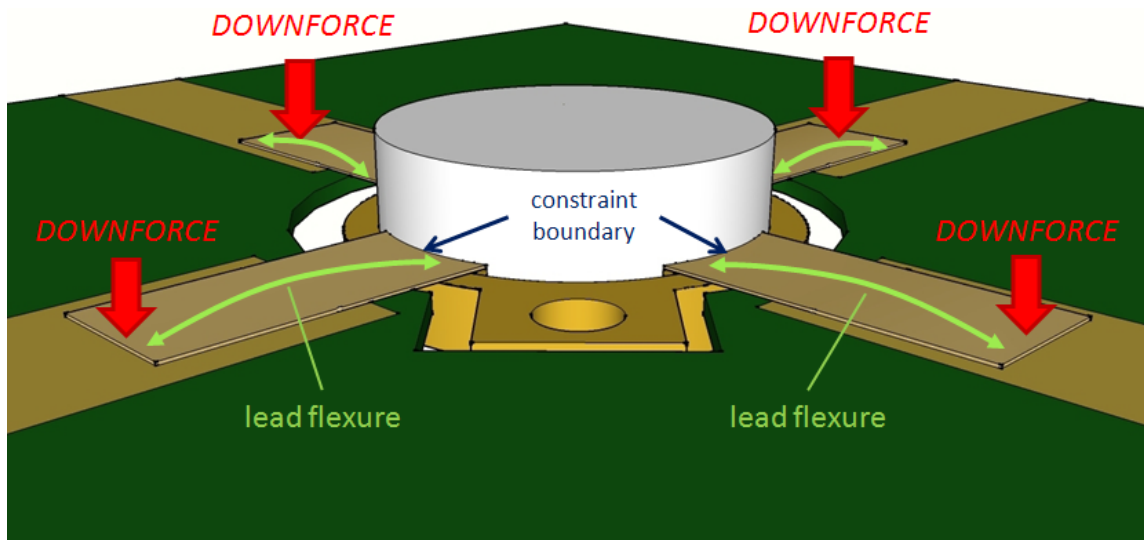


Figure 3.3 – System movement under thermal cycling leading to lead flexure.

A more likely scenario is that the downforce provided by the clamping mechanism is sufficient for reliable electrical contact, but allows for movement of the device leads with respect to the PCB due to lead, as shown in Figure 3.4. The difference in x-axis and y-axis CTE between Rogers 3210 PCB laminate and the Kovar transistor lead is $8.5 \text{ ppm} / ^\circ\text{C}$, translating to a movement of $5.1 \text{ }\mu\text{m}$ for a nominally 12 mm lead and a typical thermal excursion of $50 \text{ }^\circ\text{C}$.

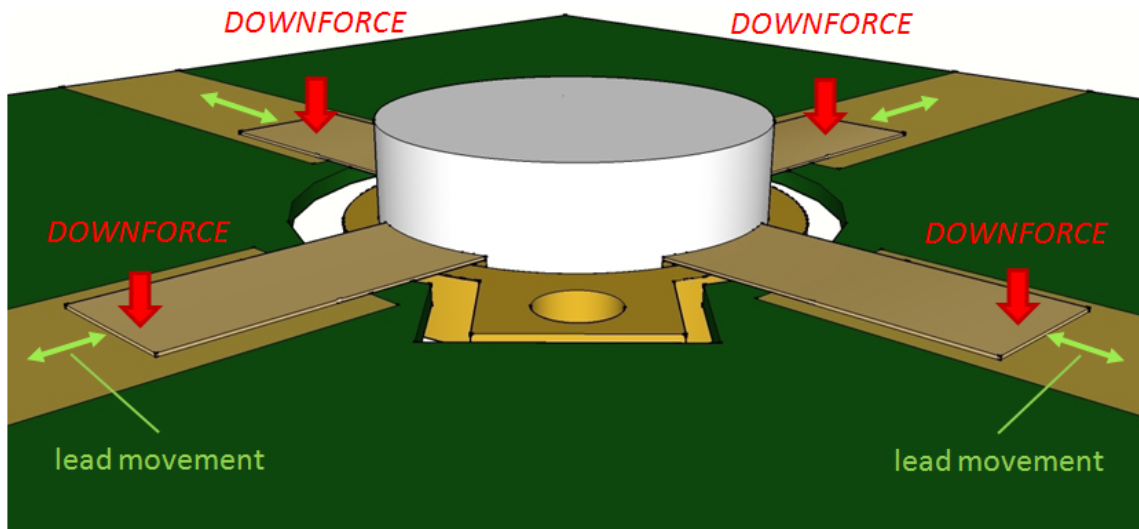


Figure 3.4 – System movement under thermal cycling leading to lead movement.

The three regimes of contact motion can be summarized as [23]:

1. Stick ($1\ \mu\text{m}$ range) – Movement between the contact surfaces is accommodated by elastic deformation of the contacts and no surface damage is incurred until unmating of the contact. This usually occurs for movements in the $1\ \mu\text{m}$ range depending on materials and contact geometry.
2. Mixed stick slip (5 to $10\ \mu\text{m}$ range) – There is a central stick area surrounded by a slip region in which some wear may occur.
3. Gross slip (10 to $100\ \mu\text{m}$ range) – All asperities and contacts are broken during each cycle.

The expected contact motion regime in which this system will operate is in the mixed stick slip regime. Movement of the device leads at this magnitude will cause wear and will have negative effects on the long term contact resistance, as will be explored further in this chapter.

3.2 Asperities

Real surfaces are not smooth, but at a microscopic level are rough. Assuming a clamped connection in which the device leads do not flex but rather move with respect to the PCB, asperity can have a major impact on the long term contact performance. Asperity can be broken down into multiple categories, as shown in Figure 3.5 [24]. Errors in form will generally be accounted for in a clamped connection, as the Kovar leads, while relatively stiff, will deform under pressure, assuming the PCB is sufficiently coplanar with the leads. Waviness is a gross manufacturing error which is the most visible to the unassisted human eye, and parts with this type of asperity should be rejected and are therefore not be considered as usable. The asperities of concern are those of roughness and subroughness. The dividing line between the two types is pedantic and unimportant for the purposes of this work. What is relevant are the affects that asperity at this level has on the system.

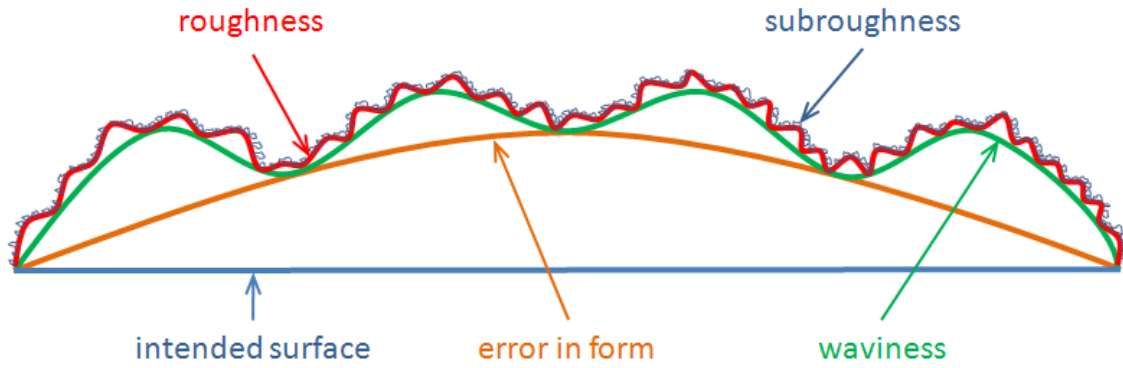


Figure 3.5 – Levels of asperity.

As two rough surfaces are brought into contact, the asperities make contact first. As the surfaces are brought closer together and the applied force is increased, the asperities deform elastically and then plastically. For analytical simplicity, if the two asperities are assumed to be spherical with different radii, the initial contact can be represented as shown in Figure 3.6, while the contact after compression is shown in Figure 3.7.

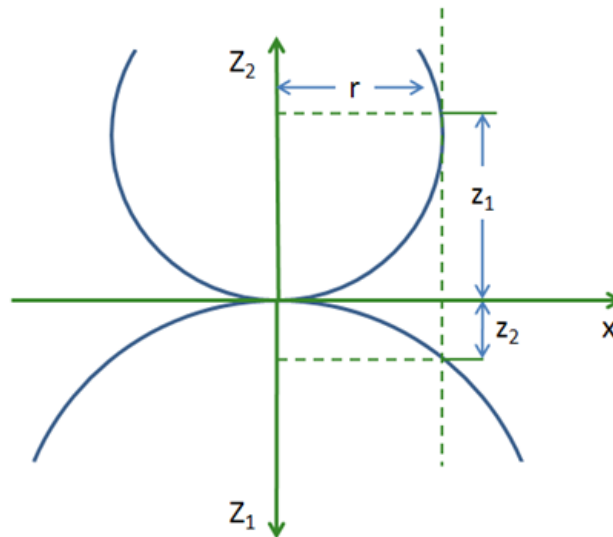


Figure 3.6 - Initial contact of two spherical asperities.

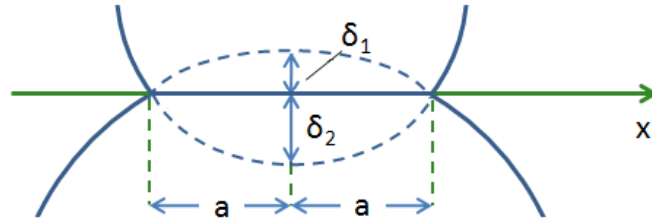


Figure 3.7 - Compression contact of two spherical asperities.

After deformation, the pre-compression distances z_1 and z_2 disappear and the asperities are deformed along the x-axis. The dashed lines illustrate the respective compressions in the z-axis, δ_1 and δ_2 .

One parameter of particular interest is the total contact area of the two surfaces. The contact area of two perfectly smooth spheres can be derived from Hertzian classical contact theory:

$$A = \pi a^2 = \pi \left(\frac{3}{4} \frac{PR}{E} \right)^{2/3} \quad (3.1)$$

where $P = \text{total load}$

$R = \text{effective radius of contact}$

$E = \text{effective elastic modulus of materials.}$

However, Equation (3.1) ignores asperity. The Greenwood – Williamson model [25] is often for used rough surfaces to include the effects asperities. The distribution of asperity summit heights $\phi(z)$ must be known (normal, uniform, etc.), which calculates

the probability that the summit height z is in the range $(z, z + dz)$. The number of summits in contact is equal to:

$$n = N \int_d^{\infty} \varphi(z) dz \quad (3.2)$$

where $N = \text{total number of summits}$

$d = \text{summits with ordinates exceeding separation of mean planes.}$

It then follows that the total real contact area is equal to

$$A = \pi \beta N \int_d^{\infty} (z - d) \varphi(z) dz \quad (3.3)$$

where $\beta = \text{an empirically derived surface roughness constant.}$

This model, while providing academic rigor, is cumbersome in practice, especially if asperity distributions or a reasonably accurate estimate of β is unknown. Empirical data from representative parts is used in the place of calculated estimates.

A sample of VHF MOSFETs and PCBs were analyzed using a scanning electron microscope to qualitatively and quantitatively understand the asperities of each. The VHF MOSFETs analyzed use the Kovar / nickel / gold leads described earlier, and the PCBs had a standard 2 oz copper, with a hard nickel underplate and gold top coat. No gold sputtering was necessary, as the surfaces being imaged are electrically conductive.

Likewise, the ground path was provided by the electrically conductive underside of each sample. The instrument used was a Hitachi S-2700, maintained and operated by the Colorado State University Surface Analysis Laboratory.

Figure 3.8 is an SEM micrograph of the lead surface of a ST Microelectronics SD2933 VHF MOSFET. The x-axis and y-axis asperities are on the order of tens of μm , while the z-axis asperities are approximately one order of magnitude lower. The mating surface in a clamped connection, a PCB trace, is illustrated in Figure 3.9. As in the MOSFET lead image, the x-axis and y-axis asperities are on the order of tens of μm . The z-axis asperities appear to be physically smaller than those noted on the MOSFET lead, likely on the order of hundreds of nm. Considering the total x-axis and y-axis dimensions of both surfaces, the x-axis and y-axis asperity dimensions, and their respective z-axis asperities which are one to two orders of magnitude smaller, it is assumed for all practical purposes that asperity will not have an appreciable negative effect with respect to the real contact area, as the parameters are well within the bounds of 'normal' for electrically mating surfaces [26].

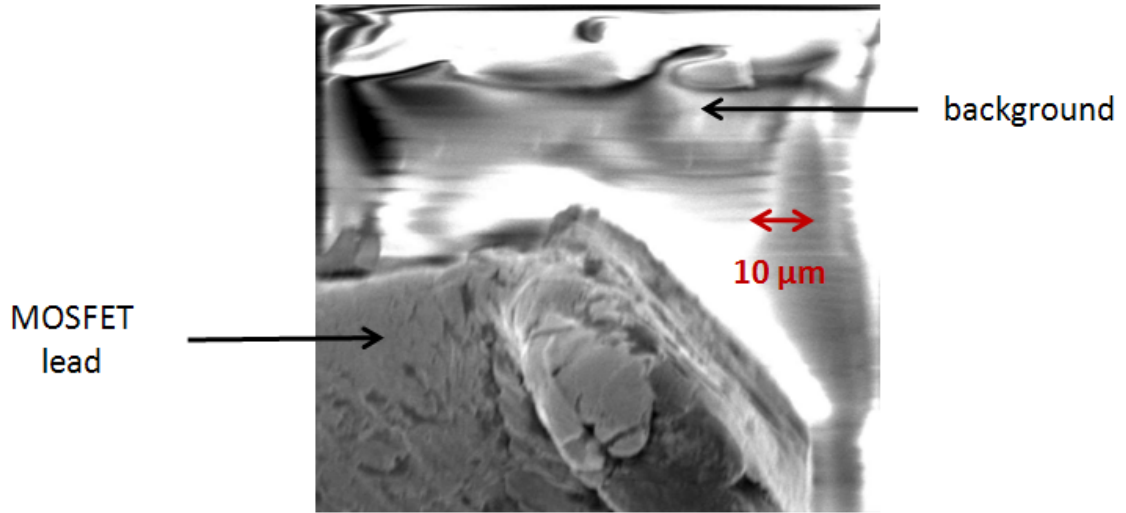


Figure 3.8 – SEM micrograph of VHF MOSFET lead surface.

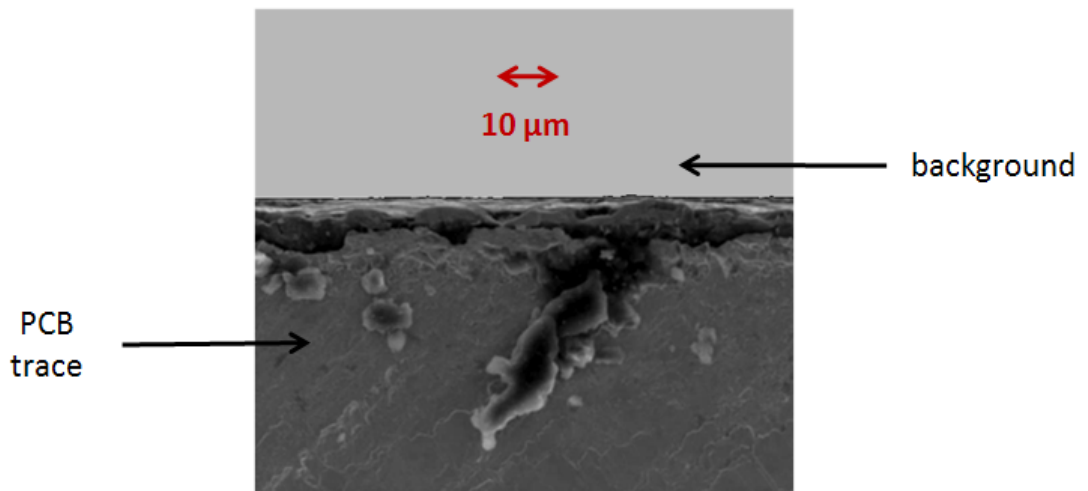


Figure 3.9 – SEM micrograph of gold plated PCB trace.

3.3 Contact wear

In a clamped electrical contact system, the combination of movement and the evidence of asperities of varying and uncontrolled magnitudes gives way to wear of the two surfaces. The basic wear mechanisms can be categorized into four groups:

adhesion, abrasion, surface fatigue, and tribochemical reaction. Adhesion involves the forming and breaking of adhesive molecular bonds between the two surfaces. Abrasion is the bulk removal or displacement of material due to scratching. Surface fatigue is the process of crack formation in the surfaces which result in the separation of material from at least one surface. Tribochemical reactions are surface interactions in which chemical reaction products which are formed as a result of tribological action. The domains and types of contact wear, along with the relative levels of intensity, are shown in Figure 3.10.

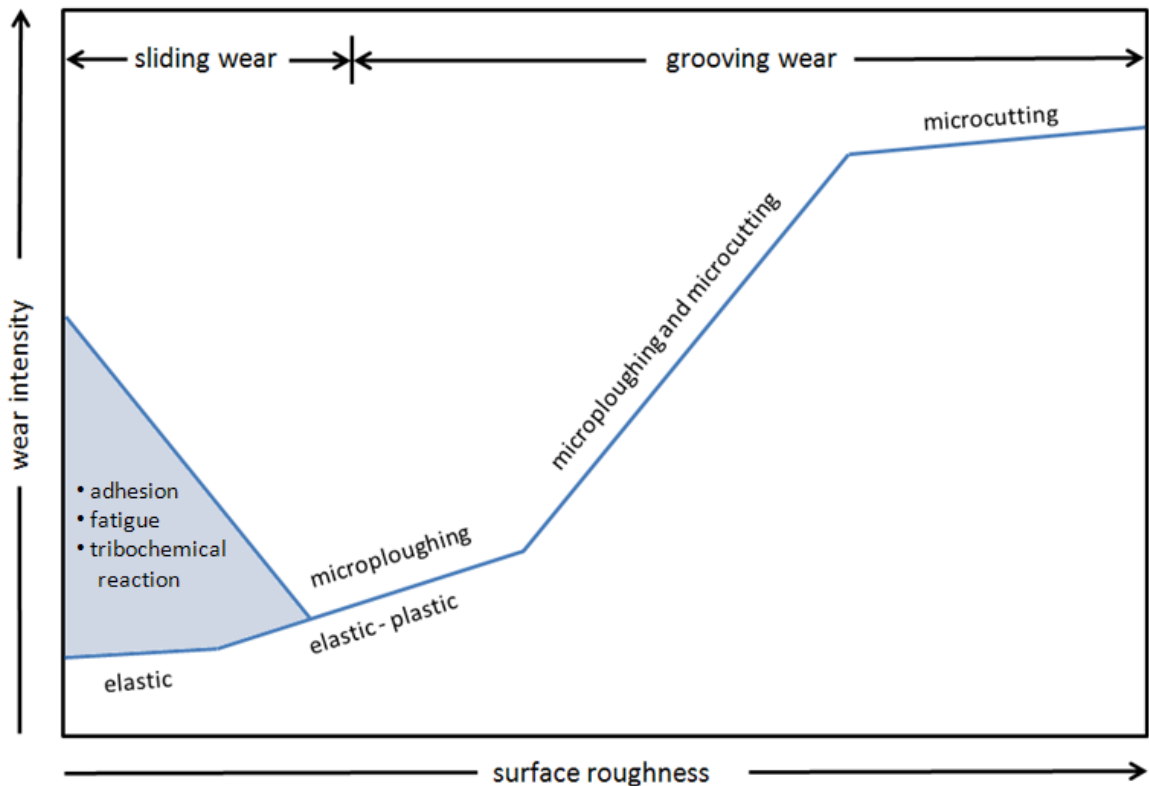


Figure 3.10 – Domains of contact wear.

Adhesion of two surfaces can occur through ionic, covalent, hydrogen, van der Waals, or metallic bonds. The dominant bonds at work in the adhesion of two metals is the metallic bond, which transpire through the movement of free electrons moving in the electronic lattice. Adhesion which takes place at room temperature and under stress levels which are nominal to the system is often referred to as 'cold welding.' Adhesive processes occur only if a surface film is not present, which may or may not be the case for gold plated leads. Oxidation is not a factor, as gold surfaces are not susceptible to oxidation, but layers as small as 5 Å of other environmental contaminants have been shown to reduce contact adhesion [27] and the preparation and cleanliness of the surfaces can dramatically affect the adhesion strength [28]. Theoretical models are available for predictive calculations of the strength of adhesive cold welded joints [29], [30]. As expected, the major factors are the amount of force applied and the available contact area.

The degree to which adhesion is a concern can also be correlated to the amount of surface energy the two mating surfaces have [31]. The atoms near the boundary of a metal surface are more disperse and hence exhibit excess energy, which increases the capacity of the surface to form an adhesive junction. The modified Dupré equation can be used to estimate γ_{ad} , the work of adhesion:

$$\gamma_{ad} = \gamma_A + \gamma_B - \gamma_{AB} \tag{3.2}$$

where γ_A = surface free energy of contacting material A

γ_B = surface free energy of contacting material B

γ_{AB} = surface free energy of formed interface.

For an interface which is gold on gold, γ_A is equal to γ_B , which are on the order of 1.2 J/m² and the contribution of γ_{ad} is on the order of 1/50th the magnitude of the individual surface free energies. This yields a theoretical maximum value of 2,000 N/mm²; experimental results are about one order of magnitude lower, likely due to practical surface cleanliness and roughness constraints. There are also limitations of exclusion in this model, particularly the lack of consideration for contact duration and temperature, which are important factors in this application. Nonetheless, an adhesive junction with a surface energy on the order of 100 N/mm² is still very strong, and must be considered in the context of this work.

Abrasive wear is defined as wear due to hard particles or protuberances forced against and moving along a solid surface [32]. Abrasion is associated with the ploughing or cutting of a surface by particles and/or asperities. The cutting points can be embedded in one or both of the surfaces or may be particles which have been removed from one or both of the surfaces through sliding wear mechanisms. These two types of abrasion are referred to as two-body and three-body abrasion, and are illustrated in Figure 3.11 and Figure 3.12 respectively.

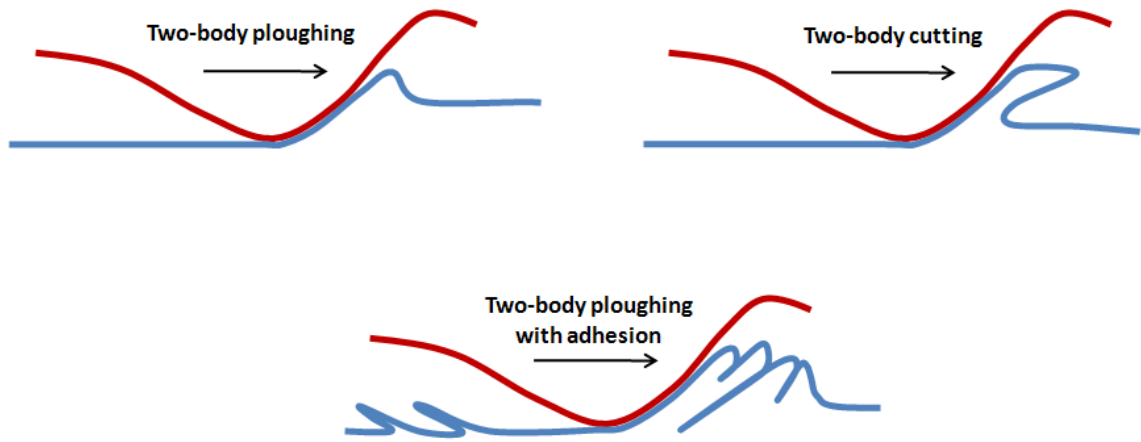


Figure 3.11 – Two-body abrasion mechanisms.

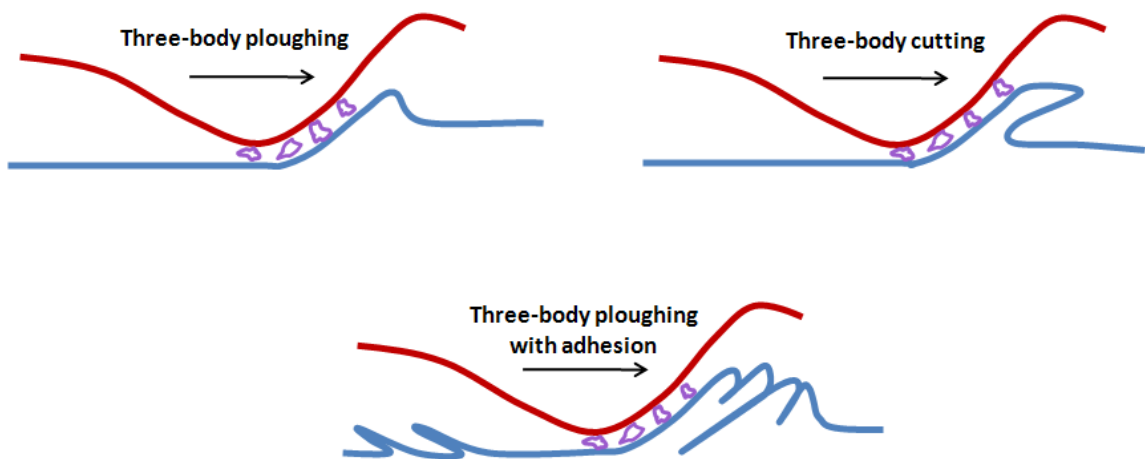


Figure 3.12 – Three-body abrasion mechanisms.

Adhesion has been shown to be a wear mechanism for the clamped electrical system under analysis, narrowing down the specific mechanisms to either two-body or three-body ploughing with adhesion. With respect to the formation of wear particles, the ratio of Young's modulus, E , and the surface hardness, H , is referred to as the critical attack angle. This measure describes the angle above which the transition

between ploughing and cutting occurs; the higher the value of E/H , the larger the critical attack angle. The system under analysis has an angle between the two surfaces of approximately 0° , suggesting that independent of the probability that wear particles will be formed is low. The abrasion mechanism at work in this system is in the form of two-body ploughing with adhesion.

The volume loss due to adhesion wear in sliding contact can be calculated as

$$W_V = \frac{skF_N}{H} \quad (3.4)$$

where $W_V = \text{volume loss due to wear}$

$s = \text{sliding distance}$

$k = \text{coefficient of wear}$

$F_N = \text{normal force}$

$H = \text{hardness of the stressed material}(s).$

The coefficient of wear expresses the probability of forming wear particles, which is best determined experimentally. In the absence of data specific to the tribosystem under analysis, an estimation of $k = 10^{-6}$ can be used [33], as this value is correlated to the transition between the stick and mixed stick slip contact regimes. Inserting values from the contact system under analysis, figures on the order of $0.1 \mu\text{m}^3$ are the result. Like other simplified models, this calculation has limitations, such as the major assumption that all wear cycles will produce particles of equal size as opposed to a progressively smaller size, which would be expected. As a relative measure to gauge the severity,

however, the model is useful. For the system under analysis, it represents another parameter which is of concern regarding long term connection degradation.

Surface fatigue is another wear mechanism of interest. It is characterized by crack formation and / or the flaking of material caused by the repeated movement or loading of the surfaces. Depending on the ductility and hardness of the materials involved, surface fatigue may occur initially beneath the visible surface. If the conditions are sufficiently severe, fatigue cracks which propagate to the surface may appear. The types of systems which experience surface fatigue include

1. Rolling of a circular body on a stationary surface
2. Ball and roller bearings
3. Pinching of a flat surface between two circular bodies
4. Impact of one surface on another
5. Fluid or dry aerosolized particulate impacted on a surface
6. Flat surfaces with an applied normal force and parallel movement, as illustrated in Figure 3.13.

Only the last of these examples are relevant to a clamped electrical connection. Furthermore, the relatively low amount of pressure (on the order of 2 MPa.) on the surfaces and the relative hardness of the substrate materials (Kovar transistor leads and a ceramic PCB) implies a situation in which surface fatigue is unlikely, especially at levels which could be detrimental to the system under analysis.

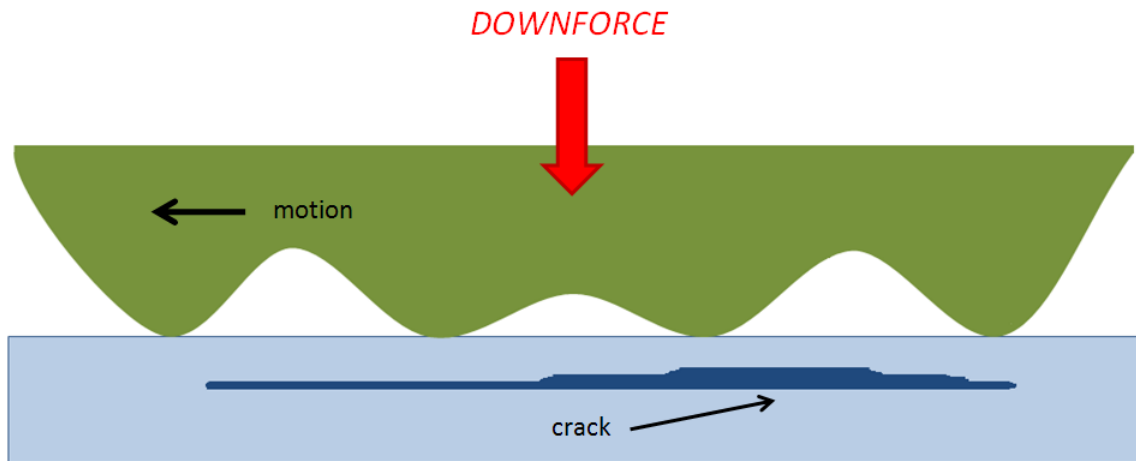


Figure 3.13 – Crack formation in sliding surface fatigue.

3.4 Corrosion

A chemical reaction causing the breakdown of a material into its constituent molecules due to interactions with the immediate environment surrounding the material is referred to as corrosion. Although other materials exhibit corrosion, this process is most commonly encountered through the oxidation of metals, which is also the reaction of concern in this work. An exposed metal surface, unless it is a metal which is naturally corrosion resistant, will eventually oxidize. Upon exposure to oxygen, some metals such as aluminum and stainless steel quickly form a thin oxide film, known as a passivation layer, which effectively prevents or dramatically slows the oxidation of the remaining bulk material.

The relevant metal elements of the clamped electrical system under consideration, namely the transistor leads and the PCB pads, are not independently susceptible to corrosion, as the contact surfaces are gold plated. However, once the system is assembled, the previously mentioned effects of lead movement, asperities,

and contact wear may eventually lead to corrosion. If, over extended usage durations, one or both of the contacting surfaces experience wear mechanisms which cause penetration of the gold plating, the underlying nickel and eventually the base metal will begin to corrode. Corrosion is rarely a desirable process, and its effects in this system are no exception.

As the corrosion progresses, the electrical resistance of the contact will increase due to the poor electrical conductivity of the oxides which are produced. It has been observed that if the oxide layer is sufficiently thick, on the order of 10 to 50 Å, a semiconductor junction may be formed, partially rectifying the signals passing through the connector [34, 35]. This action corrupts the signal, possibly to an unacceptable degree. In the clamped electrical connection system under consideration, the aggravating factor which will promote corrosion is the level of abrasion. This can be minimized in multiple ways. Ensuring that the mating surfaces are without roughness and subroughness, and limiting physical movement of the device leads are the most viable means of minimizing corrosion. In addition to decreasing wear, certain contact lubricants can also provide a very effective means of controlling oxidative corrosion, but their practical application often compromises manufacturability.

CHAPTER 4 - ANALYSIS OF AVAILABLE MATERIALS

To meet the requirements outlined in Chapter 2, material selection must be undertaken with care. The designs for clamping mechanisms can take two basic paths: one which uses electrically conductive materials in conjunction with electrically insulating materials, or a concept which utilizes electrically insulating materials exclusively. There are potential benefits and drawbacks to both approaches, and in most applications, either design path can meet the system requirements. This chapter explores readily available materials which meet the requirements for at least one type of design. Exotic materials such as composites or multilayered structures are not considered here due to their inherently higher development and manufacturing costs, but would be an alternative if their properties proved to be necessary in a certain application.

4.1 - Polyphenylene sulfide

Also known by its acronym PPS or the trade names Ryton (Chevron Philips) and Techtron (Quadrant Plastics), polyphenylene sulfide is an organic polymer. This material has good characteristics, including high dielectric strength, temperature stability, and resistance to standard environmental chemicals and pollutants. Its mechanical properties are also notable; creep resistance, flexural modulus, and very good wear resistance. The combination of these properties allow PPS to be used in demanding

applications such as pump bushings, bearings, hydraulic piston rings, and automotive applications. Parts can be machined from a block or injection molded if higher quantities are needed. PPS is a lower cost alternative to other engineering thermoplastics such as polyether ether ketone (PEEK) and can be obtained with fillers such as glass or carbon fiber to tailor the rigidity. Unfortunately, PPS is also prone to fracture when compressed, as it is relatively brittle. This could be a problem for a clamping mechanism which is comprised exclusively of PPS. The concepts developed, as will be discussed in Chapter 5, require the clamping mechanism to be secured to a heat sink with a fastener, which will exert significant pressure on the clamp in the fixturing areas. To increase the likelihood of early success during prototyping, PPS was not considered a viable material for this reason.

4.2 – Polyetherimide

PEI is another thermoplastic which shares all of the desirable electrical, mechanical, manufacturability, and cost aspects of PPS without the issue of brittleness as noted in PPS. Also known by its trade name Ultem (Sabic), PEI is also highly flame resistant and when ignited, emits very low amounts of smoke. These positive characteristics are noteworthy in the field of high power electronics, where device failures often result in large amounts of heat dissipation and potential for material ignition is a concern. PEI also exhibits comparable tensile strength to PPS, while having a flexural modulus of approximately 20% less. This allows PEI to bend under load more easily, allowing a clamping mechanism to absorb more of the mechanical stackup issues

as noted in Section 2.8. The behavior of PEI over long time periods, including degradation mechanisms, acceleration methods, and predicted failure modes are well documented [36-46]. These additional properties make PEI an excellent candidate for an electrically insulating clamp.

4.3 – Spring steel

For a clamping mechanism which is comprised of a metal structure and an insulating sheet, spring steels are a natural choice. These medium to high carbon steel alloys have a very high yield strength, allowing them to maintain force under constant load for extended periods of time. ASTM grade A666 is particularly attractive for the intended application, as it is a spring-tempered stainless steel with a yield strength of 1.01 GPa. One of the major failure modes of steel is hydrogen embrittlement [47-50], with the critical point for susceptibility at approximately 1 GPa. Regardless, environmental hydrogen does not exist in sufficiently high concentrations to promote embrittlement, and the system under analysis will not be exposed to high concentrations of hydrogen gas. The design of a clamping mechanism using any type of steel need to take fatigue and creep into consideration [51-55], but the constant loading in this specific application is unlikely to present a challenge.

4.4 – Beryllium copper

An alloy of copper with up to 3% beryllium, this material exhibits similar properties to A666 spring-tempered stainless steel, with an even higher yield strength of 1.4 GPa. In this application there are no negative implications to using beryllium copper

instead of spring steel except for the cost increase of fabricated parts of roughly 20%. Fatigue is the predominant failure mode for beryllium copper in this application, but annealing can increase the long term performance [56-59], albeit at a higher cost.

4.5 – Polypropylene

This common polymer is used in a wide variety of applications, including synthetic clothing fibers, packaging materials, laboratory equipment, containers, and as a capacitor dielectric. Polypropylene has good electrical characteristics and is resistant to creep under moderate loads [60]. Its prevalence makes polypropylene readily available and inexpensive, and the long term aging characteristics are favorable [61]. While not an acceptable material for a clamping mechanism, polypropylene is a good selection for providing an insulating layer between a metal clamp and the PCB.

CHAPTER 5 - CONCEPTS FOR ATTACHMENT

The materials discussed in Chapter 4 - are used to construct three dimensional CAD models which can be implemented into physically realizable concepts. These concepts differ in approach and all have benefits and drawbacks. Two preferred concepts are selected for further analysis.

5.1 – Single lead

This design is the simplest of the four presented. A piece of material which has been cut away at the undersides, as shown in Figure 5.1, is the member which exerts pressure on the transistor leads. This clamp is affixed through holes in the PCB and into threaded holes in the heat sink with two fasteners. The complete system is illustrated in Figure 5.2.

One benefit of this method of attachment is the latitude in material choice. As each of the four clamps only make physical contact with one device lead, they can be constructed of electrically conductive material if desired. This opens up a large amount of options such as brass, stainless steel, and copper. This flexibility can also relax cost constraints, as relatively inexpensive metals may be suitable. Electrically insulating materials may also be used without negative effect. Another benefit is in the form of mechanical tolerance stackups. As one clamp is only required to exert pressure on one

lead, the constraints for alignment between clamps do not exist. This has the effect of relaxing part tolerances and potentially making the manufactured parts less costly.

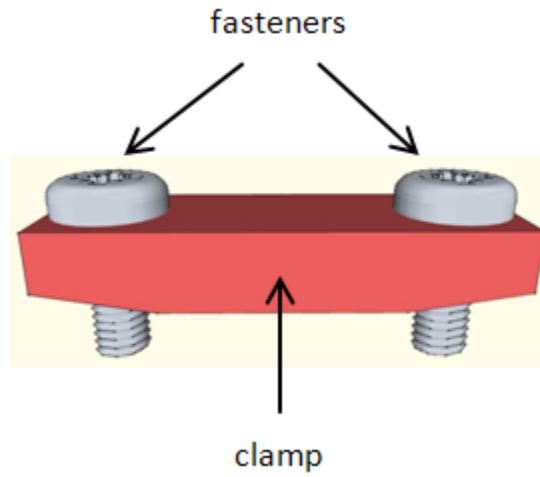


Figure 5.1 – Isometric view of clamp for single transistor lead.

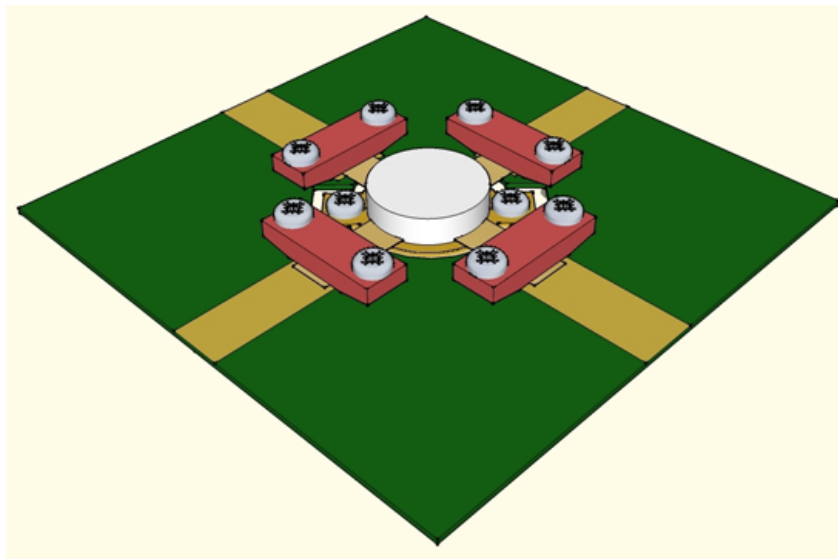


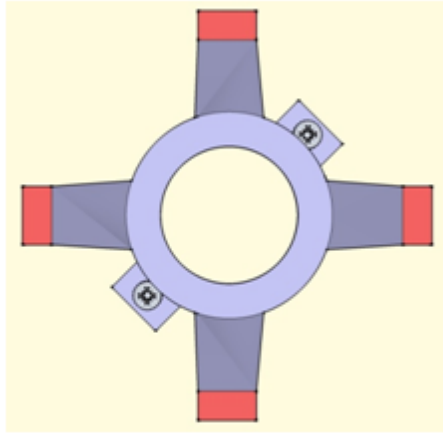
Figure 5.2 – Four single-lead clamps in the system.

A disadvantage however, is the loss in manufacturability when these clamps are assembled into a system. To make the electrical contact this concept requires four separate steps for placement of the clamps, and the tightening of eight fasteners. In addition, the mechanical connection requires an additional two fasteners, for a total of ten fasteners per transistor. As mentioned in Section 2.2, there are quantifiable benefits to having as few steps as possible. In this concept, the opportunities for human induced error are high. The manufacturability drawbacks alone are enough to prevent this concept from serious consideration in a high reliability product.

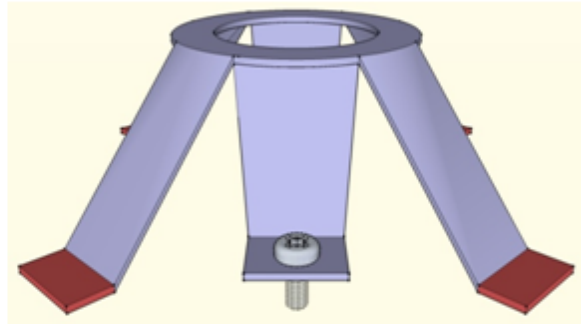
5.2 – Metal frame, insulating tabs

The metal frame clamp with insulating tabs utilizes a single piece of metal, preferably beryllium copper or stainless steel, with an electrically insulating material on the extremities of the clamp which contact the transistor leads, as illustrated in Figure 5.3. This clamp is mechanically attached to the heat sink with fasteners. The electrical contacts are made via the four beams with insulating tabs, which are slightly longer in the vertical axis than the two beams which accept the fasteners. This small difference in the vertical axis causes the four beams to deflect and exert downward pressure on the transistor leads, effectively creating a clamped connection. The system is shown in Figure 5.4. Regarding the electrical insulation on the tabs, this requirement can be achieved in multiple ways. The insulating material can be molded into a rectangular tube which is closed on one end and manually slid onto the beam. Alternately, the ends of the contact beams can be coated in an electrically insulating material which has been

heated to a viscous liquid state and which becomes solid at the expected usage temperature range.



Top view



Isometric view

Figure 5.3 – Metal clamp with insulating tabs.

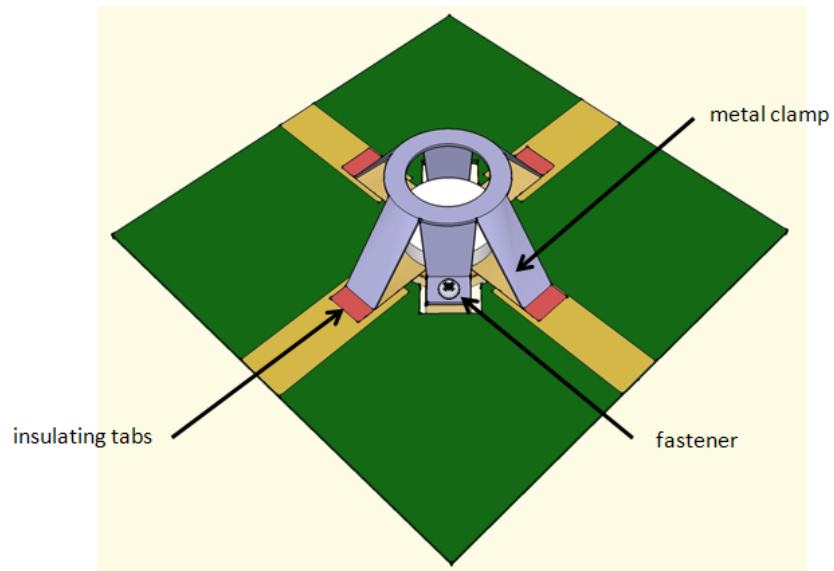


Figure 5.4 – Metal clamp with insulating tabs in the system.

There are many advantages to a clamp system which is only a single part. The manufacturability is higher than the single lead clamps, due to the usage of only two fasteners for the mechanical and electrical connection. This also decreases the opportunities for human induced error during assembly.

The negative aspects to a single piece clamp are the precision and repeatability which is required in the manufacturing of the clamp. As there are only two fasteners in the system, the relative distances between the four clamping beams and between each beam and the nearest fastener must be held to tight tolerances. If the tolerances are not maintained, problems with alignment and improper deflection of the clamping beams will be the result.

5.3 – Metal frame, insulating sheet

This design is comprised of two major components. Like the previous concept, this design utilizes a single piece of metal for the clamping mechanism. The electrical insulation is instead provided by a single piece of material, which is not part of the metal clamp. The two components are illustrated in Figure 5.5. The system is assembled in such a way that the electrically insulating sheet is placed over the transistor leads and the metal clamp is placed on top of the insulating sheet. The metal clamp is then attached to the heat sink with fasteners, similar to the previous concept. Clamping pressure is exerted on the transistor leads through deflection of the four beams. The system can be seen in Figure 5.6.

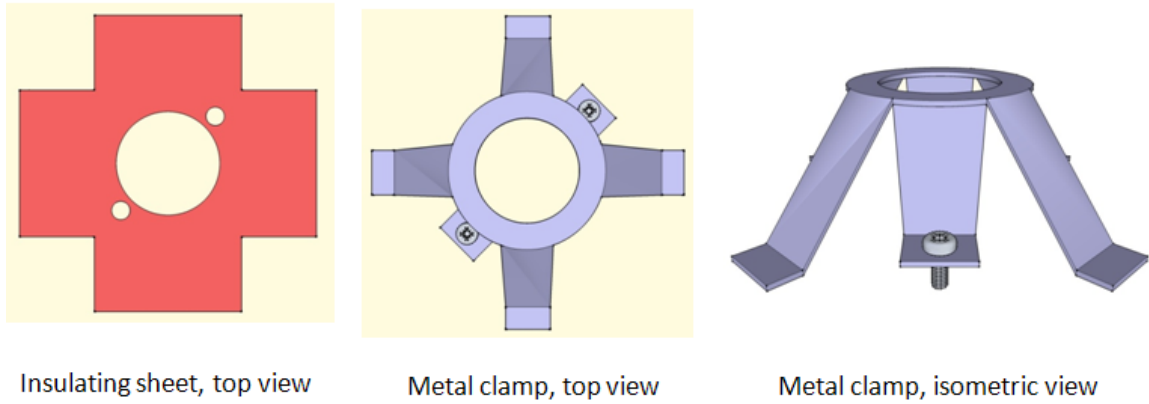


Figure 5.5 – Insulating sheet and metal frame clamp components.

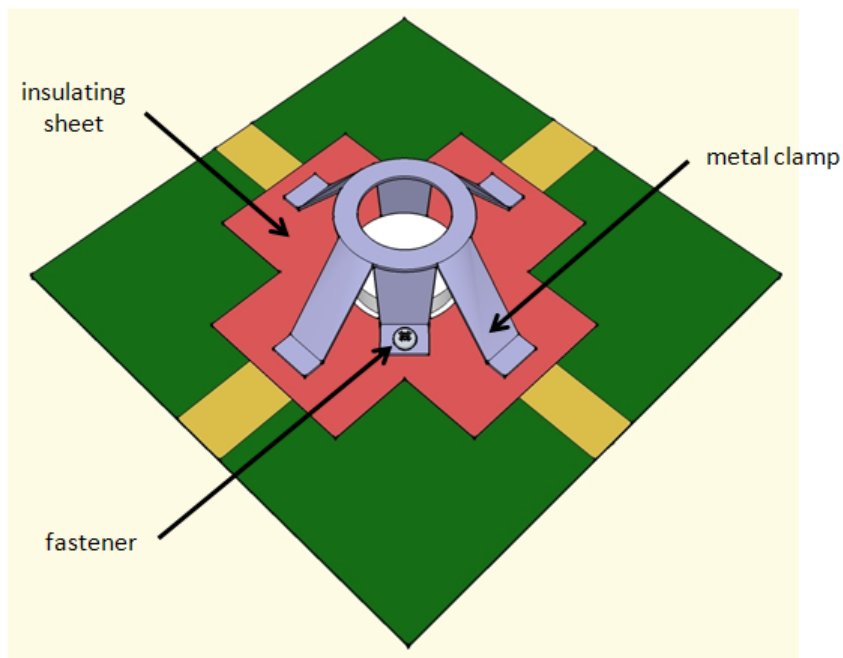


Figure 5.6 – Metal frame clamp and insulating sheet in the system.

The electrically insulating sheet is preferably cut to the necessary size with a steel rule die for precision and repeatability. The sheet material must be relatively flexible, as it needs to deflect downwards from the pressure exerted by the metal

clamp; a material which is too stiff will not absorb minor height differences in the PCB and transistor lead dimensions in the z-axis. Materials such as polypropylene, polystyrene, or an aramid provide the necessary flexibility and electrical insulation.

Benefits which can be realized with this design are possibly a lower cost as compared to the metal frame with insulating tabs. This is due to the inherent complexity in attaching molded insulators or coating the four contact beams in the previous design.

The two disadvantages of this concept with respect to the metal frame with insulating tabs are quite minor. The addition of the insulating sheet is one more step during assembly, which reduces manufacturability. This effect is small, if not negligible, as a properly designed part would self-align and have no specified top or bottom surface. Furthermore, it would be immediately obvious if the part was accidentally not included in the system. The second disadvantage is the need for two parts, the insulator and the metal clamp, to have relatively precise tolerances; the metal clamp with insulating tabs only required this of one part. There is the potential for this to increase cost, but a detailed expense and sensitivity analysis would need to be carried out to determine if this cost increase was tolerable from the overall product level.

5.4 – Insulating frame

The electrically insulating clamp is comprised of a single piece of material, preferably an engineering polymer as discussed in Chapter 4. Similar to the two previous concepts, this design utilizes a single piece for the clamping mechanism, as

seen in Figure 5.7. Like the two metal clamps, this concept is attached to the heat sink with fasteners. Clamping pressure is exerted on the transistor leads through deflection of four cantilevered beams. The system is illustrated in Figure 5.8.

Of all the concepts, the insulating clamp has the most advantages. It requires very few steps in assembly, which boosts manufacturability. The part can be injection molded from common engineering polymers for relatively low cost per part. The insulating clamp is by design electrically insulating, so no additional parts to achieve this requirement.

The main potential drawback to this concept is the complexity in the proper design of the part. As discussed in Chapter 4, the material selection is critical. Optimizing the geometry of a clamp made from an injection molded polymer has the potential to be more difficult than the same effort when using a metal, due to the stress / strain relationships and the generally lower yield strengths available in polymers. Particular attention is necessary near the points where the beams meet the circular top of the frame, as this is where stress concentration will be the highest. Nonetheless, with proper material selection, geometry optimization, and manufacturing techniques, these challenges can be overcome.

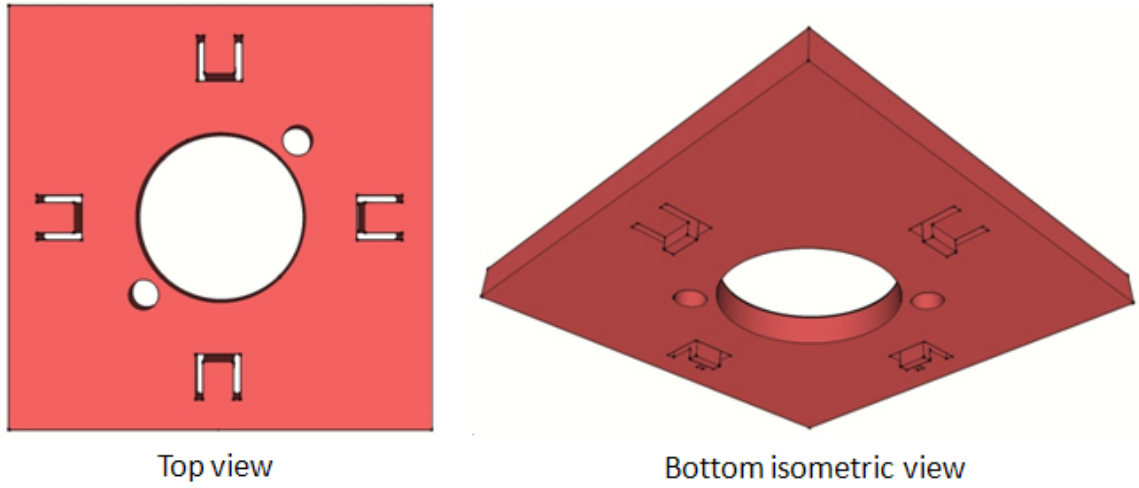


Figure 5.7 – Insulating clamp.

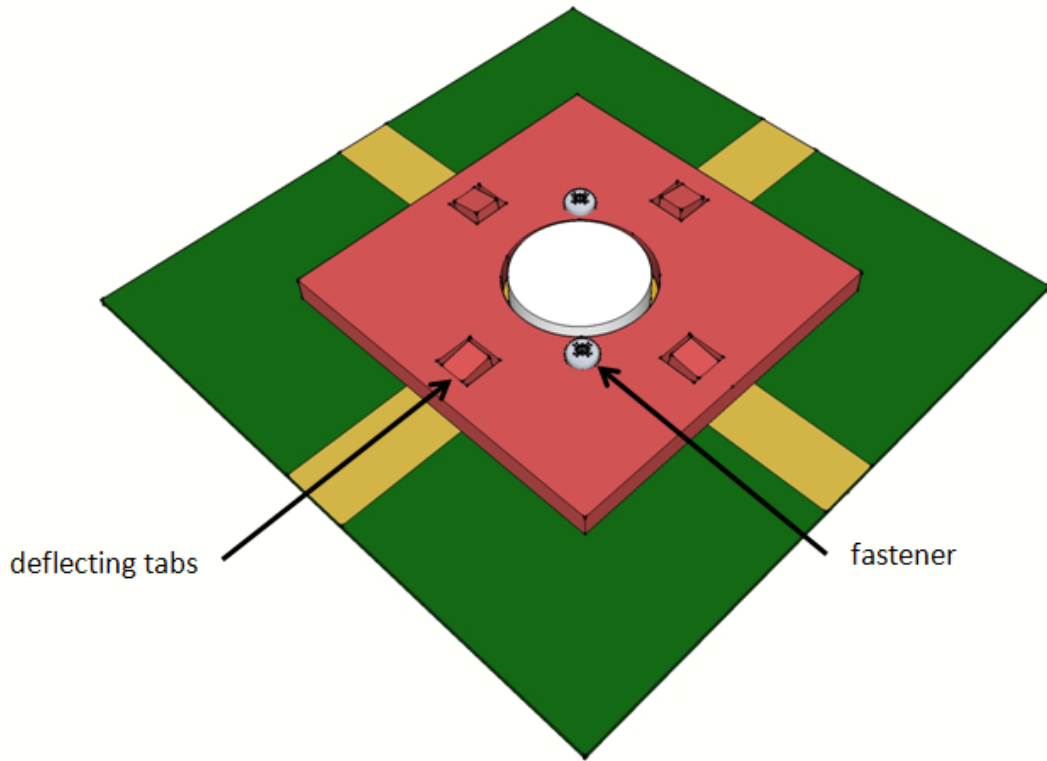


Figure 5.8 – Insulating clamp in the system.

CHAPTER 6 - EXPERIMENTAL RESULTS AND DISCUSSIONS

After weighing the many benefits and drawbacks to the four concepts discussed in Chapter 5, two designs were chosen for prototyping and evaluation, namely the metal frame clamp and insulating sheet (concept number three) and the insulating clamp (concept number four). The metal frame clamp was constructed using 0.020 inch thick beryllium copper sheet, stamped and bent with custom precision tooling. The corresponding insulating sheet was die cut from polypropylene stock in 0.030 inch thickness. The insulating clamp was injection molded using a prototype (i.e. “soft”) tool to save cost. The material used for the insulating clamp was Ultem 2300, a 30% glass filled PEI. A series of tests were performed to characterize the concepts and determine if one or both met the desired criteria.

The critical parameter for these tests was the amount of force the clamp beams could generate over a prolonged period of time. All materials will relax to some degree in a constant deflection application, and the amount of relaxation determines if a particular concept is viable or not. The other requirements, as outlined in Chapter 2, are met by design and do not require any experimentation to prove their validity. As the required absolute downforce for all clamping systems will be dependent on the particular application, the data is presented primarily in terms of percent relaxation, with the datum being the force at the outset of the experiment. The average point at which the beams of a clamping mechanism reached 70% of their initial applied force

was taken to be a comparative measure, as the data was either readily available or extrapolation through linear and/or logarithmic curve fitting was possible with reasonably high confidence in the accuracy of the predicted trend. Note that the numbering scheme of the beams for purposes of data presentation is arbitrary and do not correlate between experiments or concept types.

For these experiments, a fixture was designed and multiple pieces were fabricated out of aluminum block using CNC machining. This fixture was designed to accept load cells, transducers which convert force to a voltage output using strain gauges. The fixture also had raised features to simulate the PCB and transistor lead heights to allow for the proper deflection of the clamp beams. The load cells were a combination of models from Stellar Technology (model VLC856) and Omega (model LCMKD-100N). The load cells have self-contained instrumentation amplifiers, which were powered by a Hewlett Packard model E3631A DC power supply. The data was recorded at specified intervals using an Agilent 34970A data acquisition system and a corresponding 34901A 20-channel multiplexer module.

6.1 – Room temperature relaxation

One of the parameters which needed to be understood was the relaxation of the clamps at room temperature when under load. This is important information, as a product which uses a clamping mechanism may remain in an unpowered state for long periods of time. Room temperature data also provides the reference point to which

elevated temperature data will later be compared. One of each prototyped clamping system was secured to a fixture and left undisturbed.

Concept number three generated initial forces with a range of 1.2 to 2.6 lbf, which for this application are sufficient. Figure 6.1 shows the relaxation versus time of this concept. Of particular note is the data for beam 3, which increases with time as the others decrease. This is due to the clamp tilting toward one side, an effect of poor clamp symmetry, stress hardening of the clamp structure, a nonuniform polypropylene, or multiple causes. Multiple iterations of this experiment were performed with an assortment of clamp and sheet samples, with similar results. Extrapolating the data for beams 1, 3, and 4 yields times of 87, 129, and 150 days to reach 70% of the initial force, with an average of 122 days.

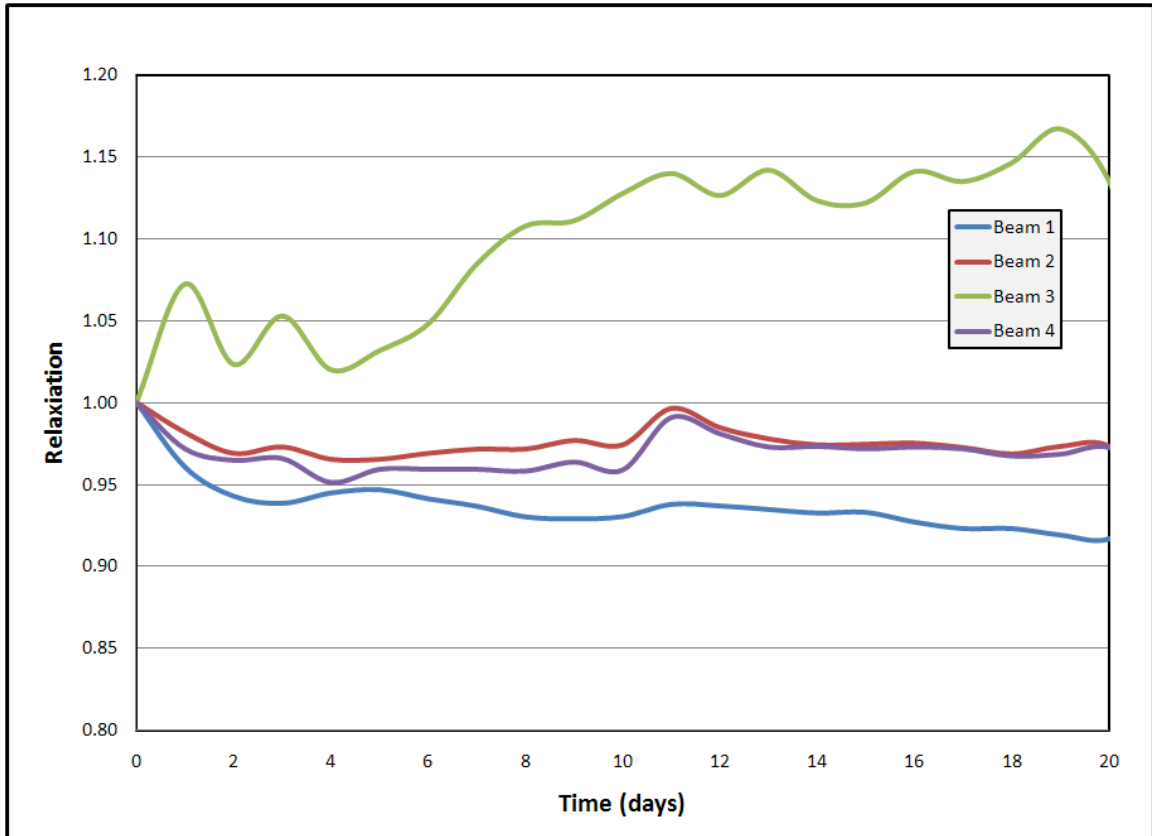


Figure 6.1 – Room temperature relaxation of beryllium copper with polypropylene insulating sheet.

Concept number four generated forces ranging from 4.6 to 6.6 lbf. The relaxation versus time is shown in Figure 6.2, which demonstrates the relatively fast relaxation during the first one to two days, followed by a decreasing rate of relaxation. Data extrapolation yields an average time of 370, 389, 425, and 430 days to reach 70% of the initial force, the average being 403 days. This concept was kept under test for a longer period of time due to the encouraging initial results.

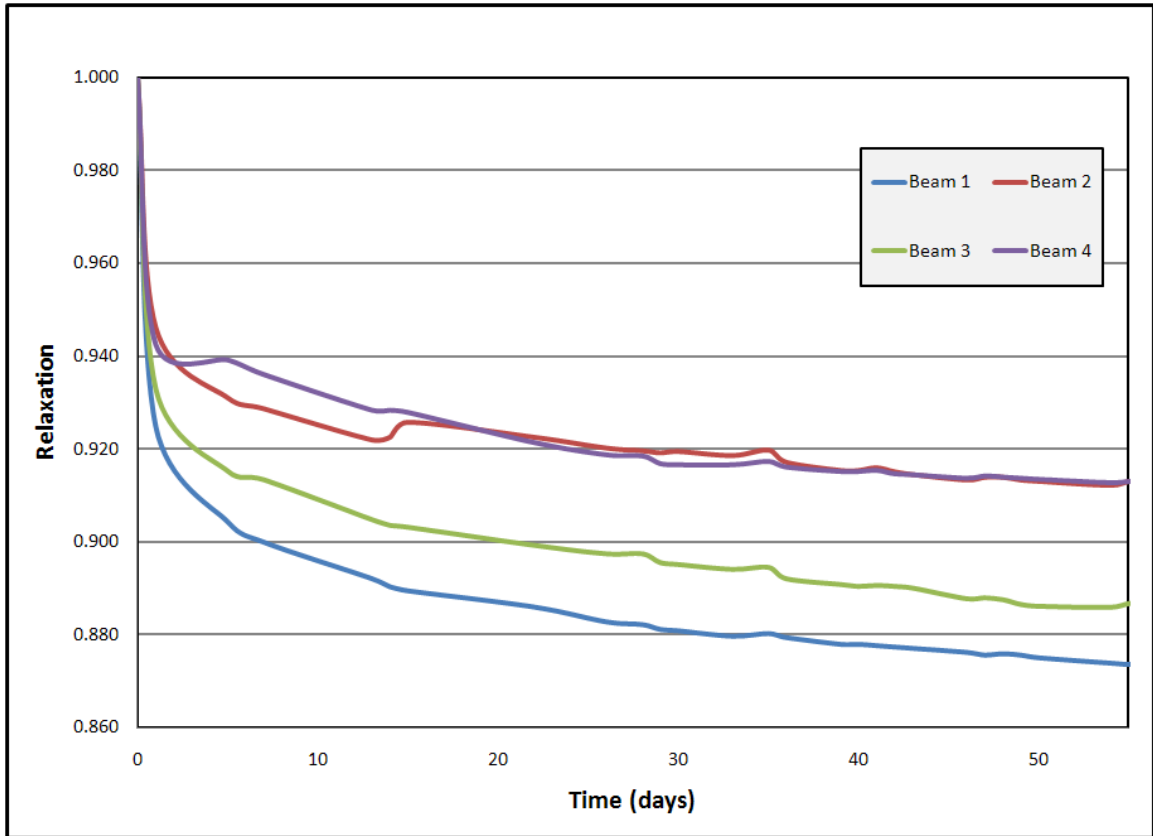


Figure 6.2 – Room temperature relaxation of Ultem clamp.

6.2 – Thermal cycling

Concept number four underwent a thermal cycling test, the goal of which was to accelerate the thermally induced relaxation effect. This allowed for quicker characterization of the relaxation behavior. Fixtures and test equipment identical to those used for the room temperature testing were used. A Qualmark Typhoon 4 environmental chamber was used to induce rapid temperature changes in the clamping system under test. The signal leads from the load cells exited the chamber through a port in one of the chamber walls. The profile which the clamping system was subjected

to, and the actual response of the environmental chamber, as measured by a T-type thermocouple affixed to the clamp surface, are shown in Figure 6.3.

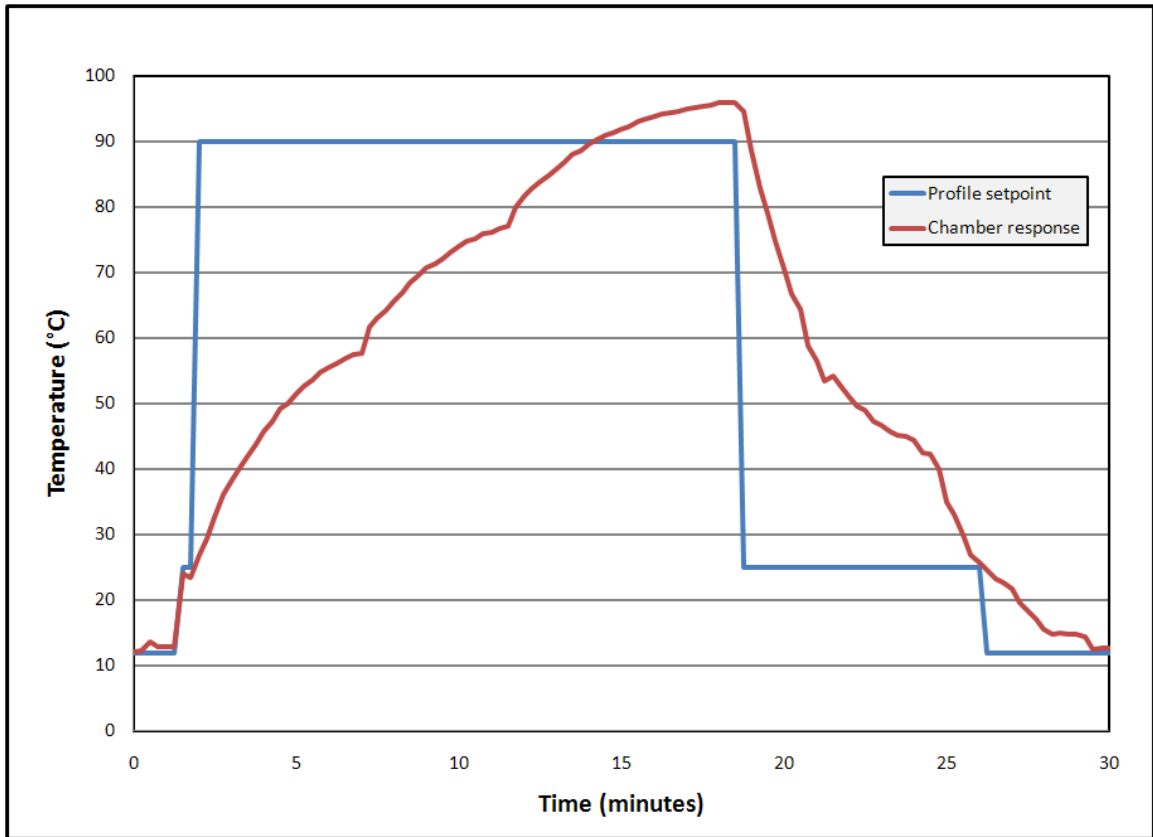


Figure 6.3 – Thermal cycling profile and chamber response.

Each thermal cycle produced a predictable increase and decreasing of forces applied by the beam onto the load cell as the temperature was cycled from approximately 12 °C to 95 °C, respectively. These changing forces are highlighted in Figure 6.4.

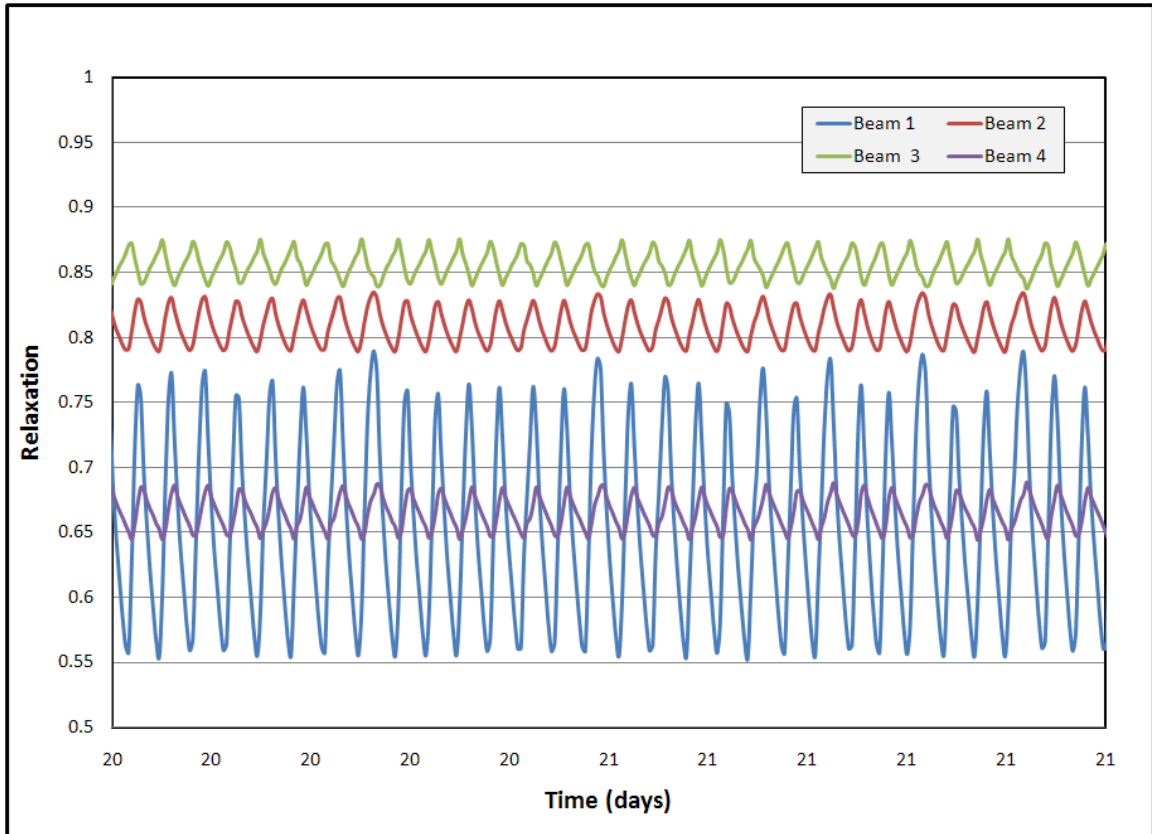


Figure 6.4 – Relaxation behavior of Ultem clamp during thermal excursions.

Due to the rapidly changing environment, data was sampled every fifteen seconds. This test was run for 47 days, and the data set required data reduction techniques to identify trends. Iterative statistical means of data samples were used to reduce the data set to a manageable size with an Excel script. The resultant relaxation trend is illustrated in Figure 6.5. Two of the beams lose 70% of their initial force during the first thermal cycle, while the remaining two lose approximately 8% to 18% of their initial force. Extrapolation of the data from Beams 2 and 3 was not performed, as there is no valid correlation between fixed temperature testing and dynamic temperature testing with respect to predictive behavior. It is clear however, that the thermal cycling

dramatically accelerates the relaxation trend and is useful for qualitatively validating the relaxation behavior in a timeframe of approximately five days. The thermal cycling data presented could also be used as a baseline for additional experiments, for example the optimization of clamp geometry or comparison of alternate materials.

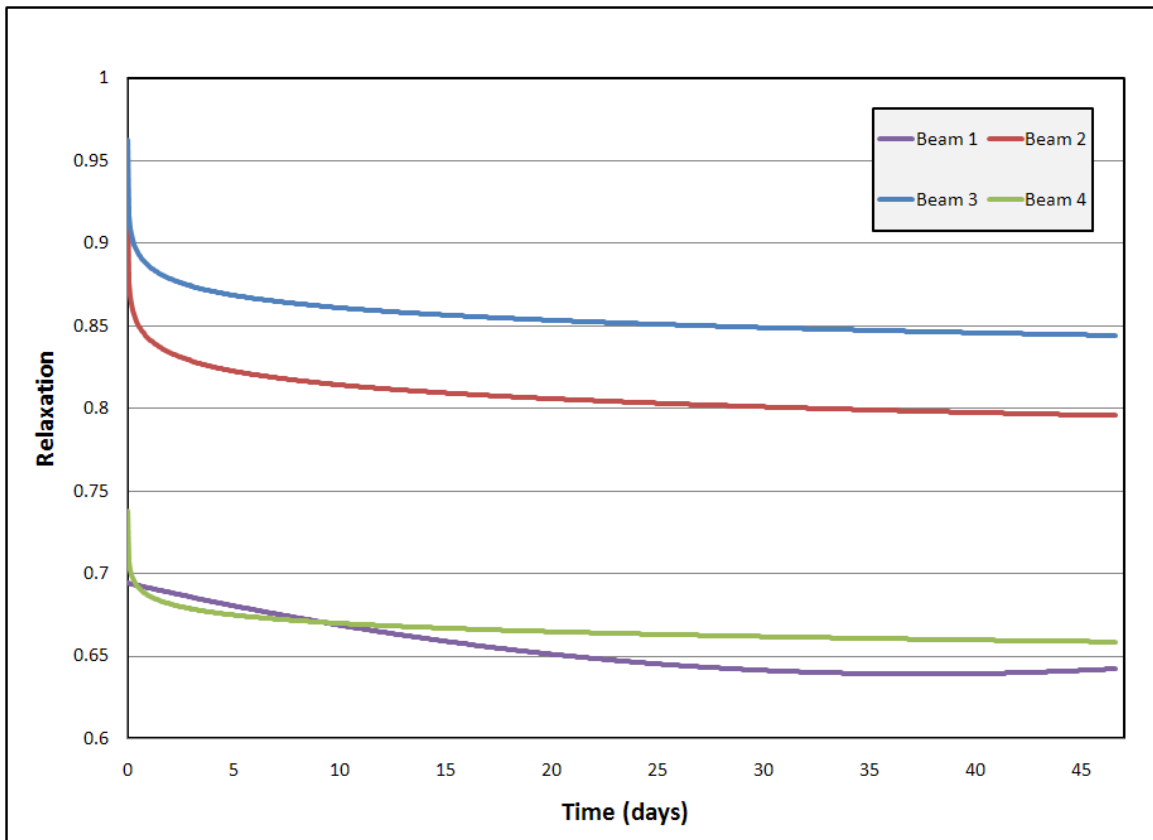


Figure 6.5 – Relaxation trend of Ultem clamp during thermal cycling, reduced data.

6.3 – Elevated temperature relaxation

To predict long term behavior, it is useful to have a steady state acceleration factor, that is a constant which correlates between different stress levels. Extensive

studies have been conducted to predict the behavior of polymers when time and temperature are variables [62-66]. To ensure that the failure modes which are dominant in the accelerated testing match those at nominal stress conditions, it is crucial to conduct the experiments at stress levels that do not radically deviate from normal usage conditions [67]. To this end, elevated temperature experiments at 50 °C and 80 °C were devised. Laboratory ovens manufactured by Binder Incorporated, model FD115, were used to elevate the operating temperature, and the fixtures as used in the room temperature analysis and thermal cycling were used. The signal leads from the load cells exited the chamber through a port in one of the chamber walls, and identical power supplies, data acquisition systems, and multiplexer cards were employed.

The data for concept three is shown in Figure 6.6. The apparent rapid decrease in clamping force is due to an error in the automated data collection script; it is assumed that the actual relaxation profile was logarithmic, as approximated by the dashed lines. The scripting was operational after about one day; data recorded after this point is correct. Also note that only data for three of the four beams is shown; one load cell was later determined to be defective and this data has been excluded. With respect to the remaining data, one beam reaches the 70% mark in less than one day. Data extrapolation of the other two beams yields times of 15 days and 194 days to reach the 70% mark, with the average of the three being 70 days. An acceleration factor was not calculated for these data sets due to the large variance. The potential for two of the beams to lose 30% of their initial clamping force in approximately two weeks, at a temperature which would be common inside a high power RF amplifier, is cause for

serious concern. This, coupled with the very wide range of data, spanning more than an entire order of magnitude in only three data points, are discouraging enough to consider this specific incarnation of concept number three unacceptable. It is likely that this concept could be redesigned to give acceptable performance, through optimization of the geometry or alternate material selection, but time and budget constraints made this impossible.

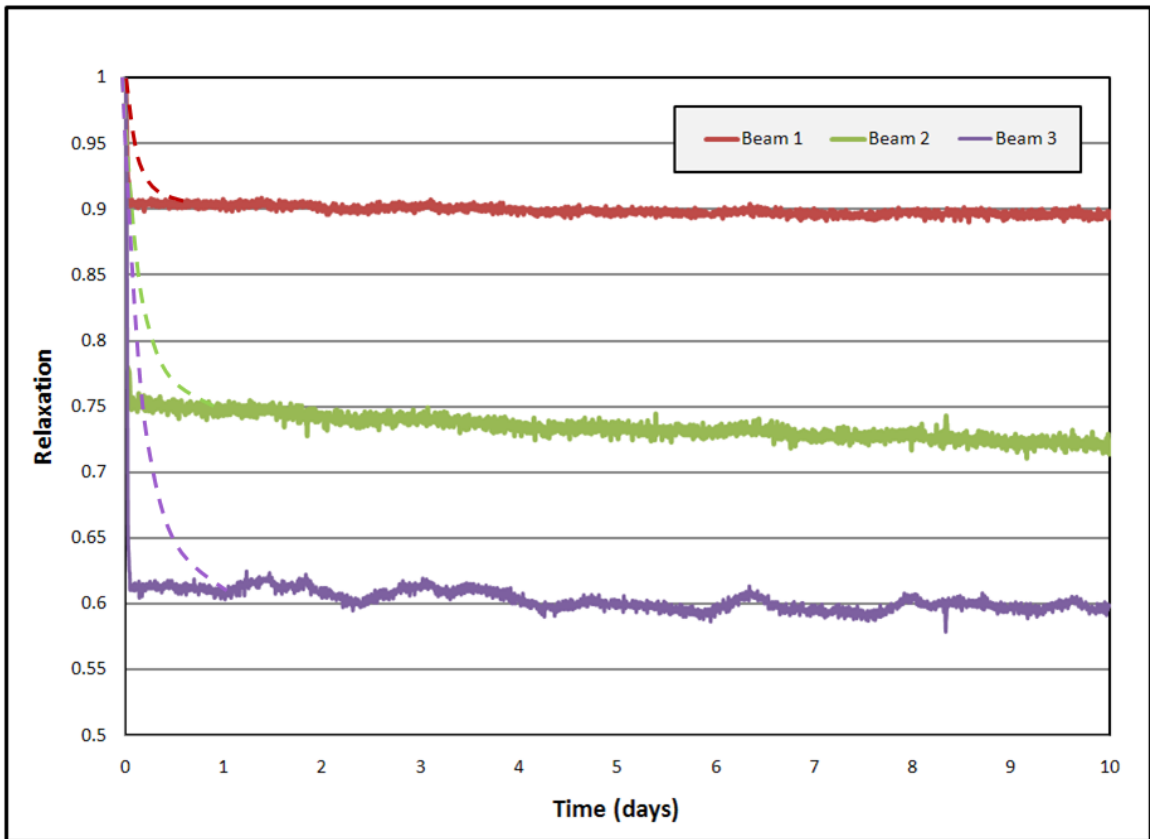


Figure 6.6 – Relaxation of beryllium copper clamping system at 50 °C.

The relaxation behavior for concept number four is illustrated in Figure 6.7. As with concept three, the scripting error affected the data and the presumed logarithmic

trends for the first day are shown with dashed lines. Two full clamps with four load cells each were used for this experiment, which explains the eight data sets. None of the beams reached the 70% mark within the ten day evaluation. Extrapolation of the data sets gives times between 54 and 81 days to reach the 70% mark, the average being 68 days. The relatively tight grouping of the data sets suggests very good consistency and predictable behavior, which are obviously desirable.

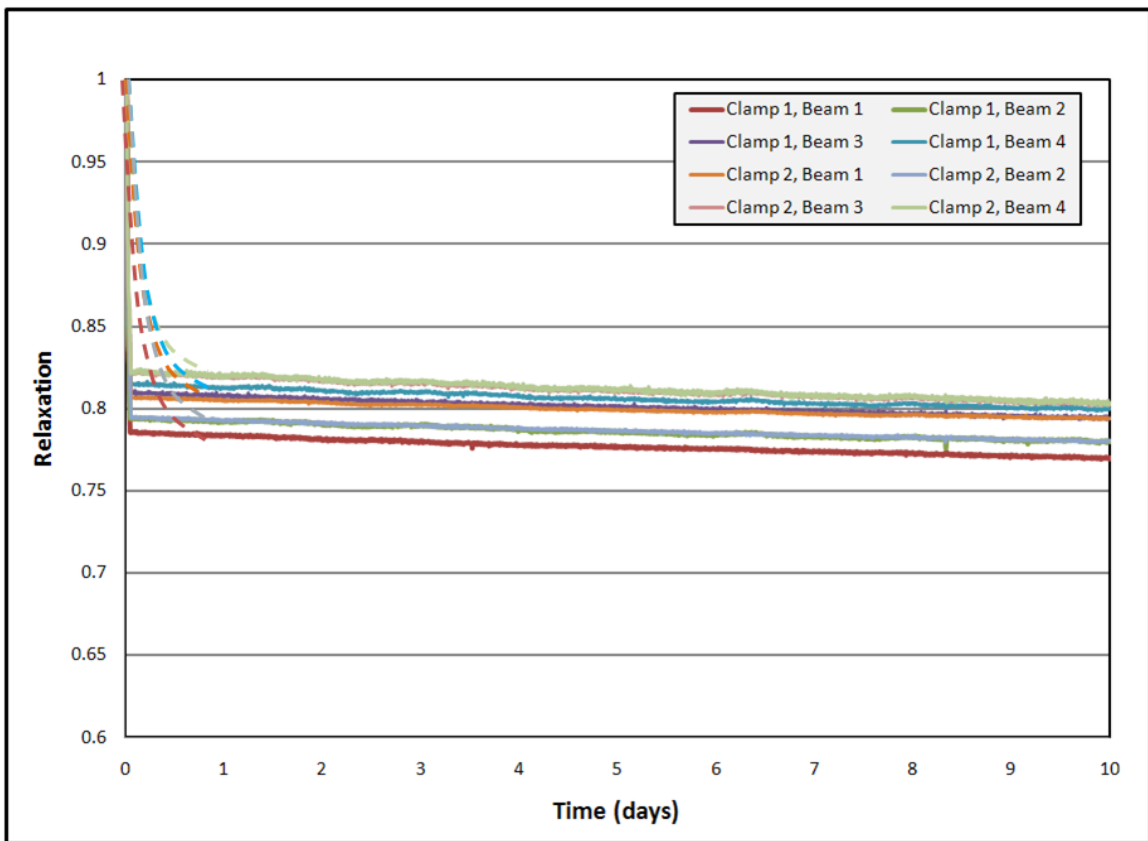


Figure 6.7 - Relaxation of Ultem clamp at 50 °C.

Because of the promising results at room temperature and at 50 °C, concept four was also tested at 80 °C, in order to provide a temperature dependent acceleration factor. The experimental setup was identical to that used for the evaluation at 50 °C.

Data for this experiment is graphed in Figure 6.8. Note that data exists for all beams at the 70% mark, requiring no extrapolation; the times recorded are 1.4, 5.1, 5.2, and 21.2 hours. The average time to lose 30% of the initial force is 8.2 hours.

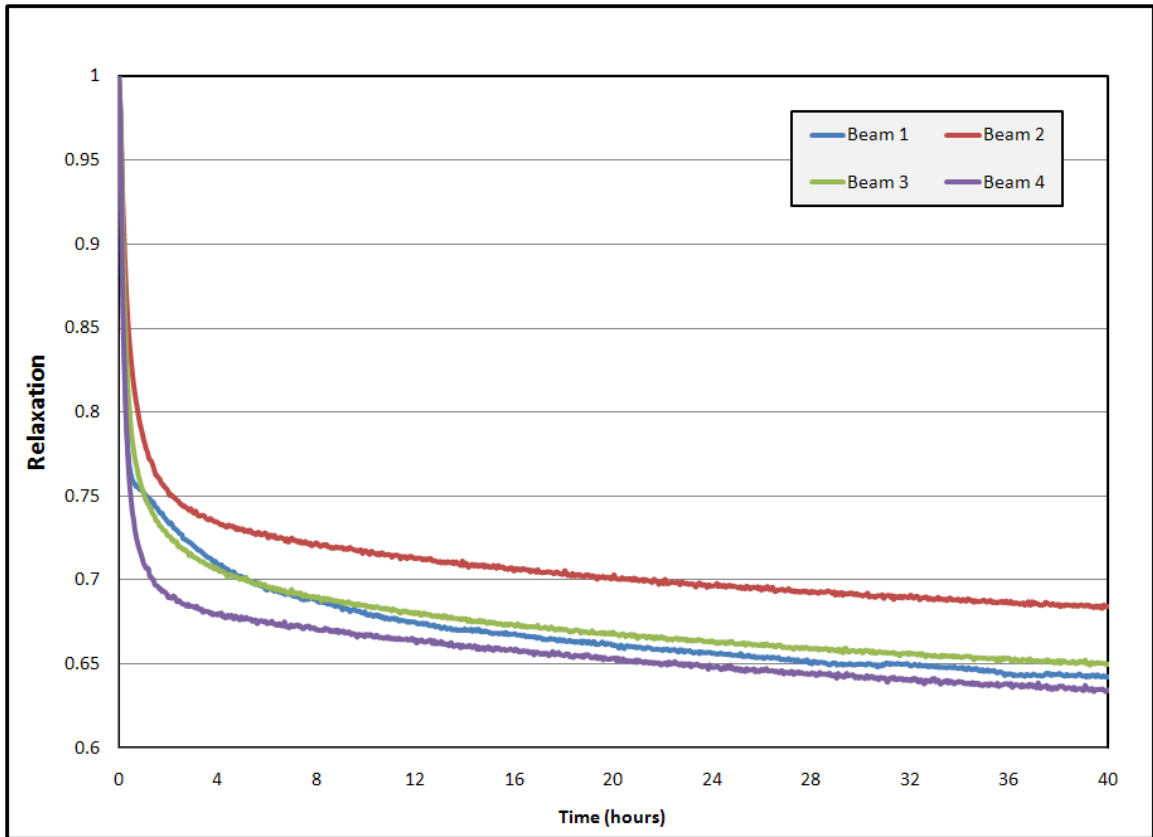


Figure 6.8 - Relaxation of Ultem clamp at 80 °C.

With data existing from experiments at three different temperatures, an acceleration factor can be estimated. At 25 °C, the acceleration factor is defined as zero, as this is room temperature. At 50 °C, an acceleration factor of 4.6 is taken from the most conservative estimate, while 6.0 is the value when the average values are used. At 80 °C, the conservative estimate is 184; the average values yield an acceleration factor of 519. It is preferred to err on the side of conservative estimates

when calculating reliability parameters and therefore the lower values are most useful. A trend can be easily seen when these data points are plotted on a log scale, as shown in Figure 6.9. The trend line is exponential with an R^2 value of approximately 0.97. This suggests that the relaxation behavior of the Ultem clamp can be predicted with statistical accuracy between the temperatures of 25 °C and 80 °C. The estimates could be extrapolated by ± 10 °C with reasonably high confidence; outside these limits, additional test data would be necessary to confirm that different relaxation behaviors were not becoming prominent.

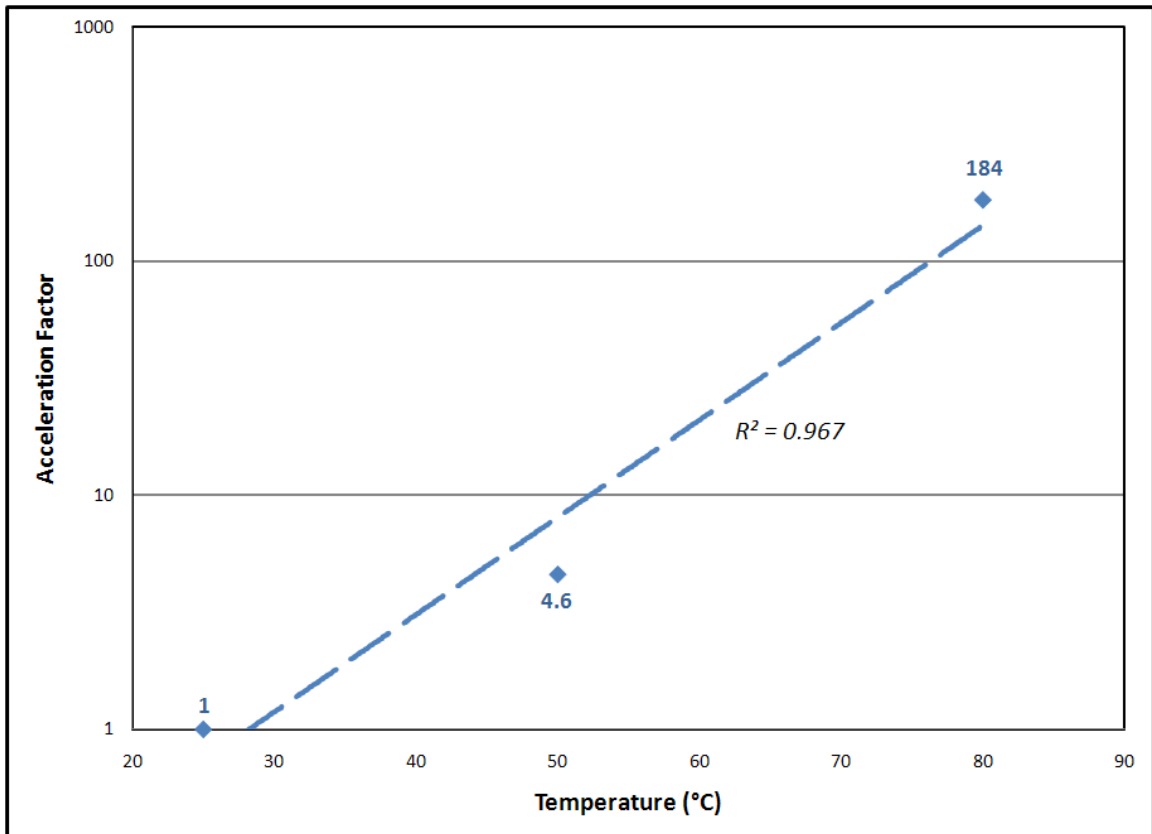


Figure 6.9 – Acceleration factor vs. temperature for Ultem clamps.

6.4 – Highly Accelerated Life Test

HALT is a process by which a new system is evaluated in terms of its operating and destruct margins through the application of stresses. These stresses are applied to the system while it is performing its intended function, in order to determine how and when it deviates from the specified performance margins. The stresses which are applied exceed those encountered in the normal usage environment, often by a fairly large margin. The benefit is that failure modes which would typically take weeks or months to appear on a large sample of units can be precipitated within hours using the HALT process.

HALT is a 'test-to-fail' evaluation, that is, the goal is to make the system fail. Following the failure(s), the useful information for the system development team is contained in how and when the system failed. Two types of limits are determined during HALT. The Operational Limit is the point at which at least one of the system's performance specifications is no longer being met. Once the stress is removed or reduced, the system again performs to specifications. The Destruct Limit is the point at which the system does not function due to damage induced by stress [68]. When the stress is reduced, the system does not operate properly and requires repair. These limits are useful in determining how much operating margin the system has and if that margin is sufficient to account for the variability in end-usage environments or customer overuse / abuse.

HALT typically has five segments, which are performed sequentially. The order is important; based on industry best practices and known failure modes, the segments

which are least likely to cause irreparable damage to an electronic system are performed first, with the likelihood of damage increasing as the test progresses. This order ensures that the most information can be gleaned from the testing before damage occurs to the system. The five segments are depicted graphically in Figure 6.10.

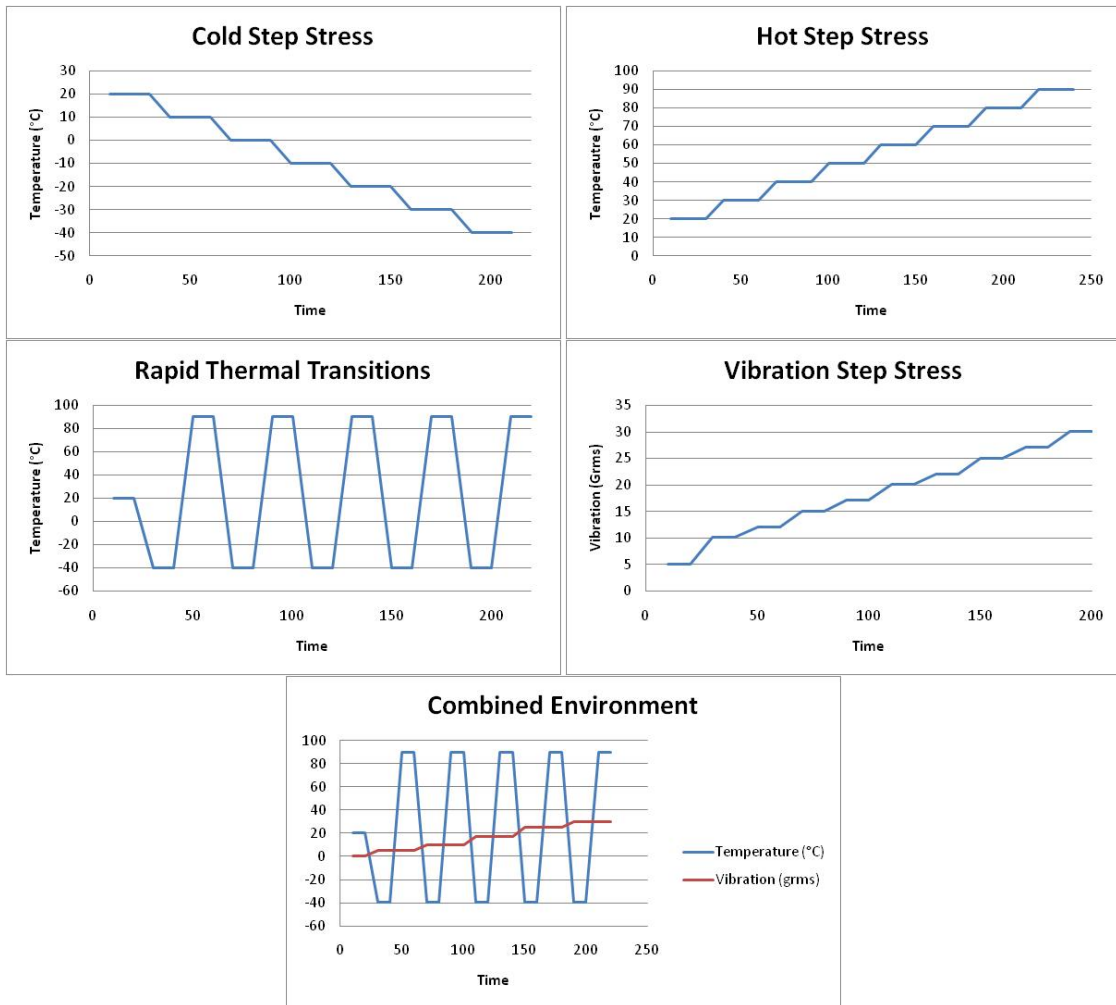


Figure 6.10 - Graphical depictions of the five HALT segments.

Cold step stress is the first segment; the system is tested at progressively lower temperatures. Hot step stress follows, using the same technique. Rapid thermal transitions is the next step, the low and high temperatures typically being set at a few

degrees inside the operational limits determined in the previous two steps. The vibration step stress is then conducted. Lastly, the system is subjected to the combined environment test, which combines rapid thermal transitions with progressively increasing vibration step stress.

Multiple pieces of clamping concept number four were used for clamping the RF transistors in two prototype VHF generators which were subjected to the full HALT sequence. The operational limits of the generator exceeded -50 °C on the low temperature end and 80 °C on the high temperature end. Thermal transitions were on the order of 60 °C/minute. No operational limits below 25 g_{RMS} were discovered before this step was aborted. Combined environment testing was conducted from -40 °C to 70 °C, and at vibration levels up to 25 g_{RMS} . No failures which were related to the clamping mechanism were noted.

6.5 – Steady state and transient thermal testing

The prototype VHF generators used in the above testing also provided a test bed for thermal testing of the clamping system. The Ultem clamp was used exclusively for this evaluation, the intent of which was to determine if the device die and the Ultem polymer clamp were being maintained at temperatures which were within their reliable operating ranges.

Figure 6.11 shows the Ultem clamp and a VHF MOSFET, which has had the ceramic protective cap removed for thermal analysis. The VHF MOSFETs used incorporate dual dice in a single package, as can be seen in this photograph. Note that

the parts have been coated with a thin layer of flat black aerosol paint to reduce optical interference with the infrared thermal camera.



Figure 6.11 – Ultem clamp and decapsulated VHF MOSFET.

A Flir Systems SC5000 cryogenically cooled high speed infrared camera was used to digitally acquire temperatures. A 320 x 256 pixel video was captured at a frame rate of 100 Hz, giving 10 ms resolution. The VHF generator had the AC mains applied and was initially running in an idle state, generating zero RF output power. Cooling for the generator was provided by water at a temperature of approximately 17 °C as measured at the inlet, at a rate of 3 gal/min and air at approximately 25 °C, at a rate of 220 f³/min. The VHF generator was then abruptly programmed to generate maximum RF output power, which is on the order of kilowatts. The thermal images extracted from the video file were then processed to extract transient and steady state temperature data. A decapsulated VHF MOSFET is shown in Figure 6.12. Each of the dice were measured

separately but were averaged for all analysis. The 'exposed bulk package' measurement refers to the blue shaded area inside circle and does not include the area of the dice.

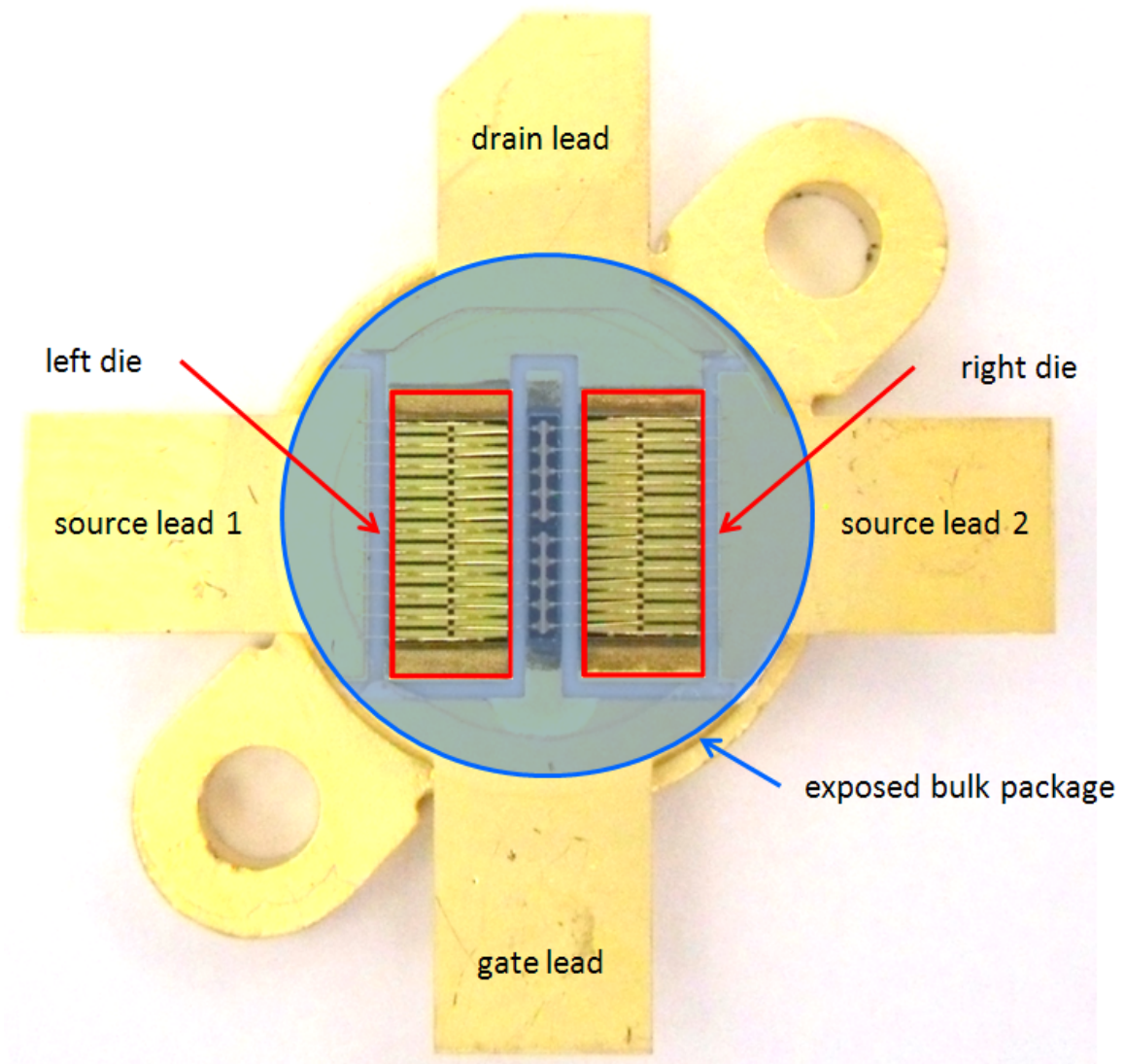


Figure 6.12 – VHF MOSFET with identifying annotation.

The temperatures were recorded for approximately 11.5 seconds after RF power was generated. Relevant temperatures for the MOSFET are illustrated in Figure 6.13.

Due to the very large radiated RF fields produced by the VHF generator when the steel chassis cover is removed, a fair amount of electromagnetic noise was coupled into the camera, causing the oscillatory behavior noted in this graph and similar graphs to follow. The change in the data pattern at the five second mark can be attributed to the camera automatically adjusting its data range for maximum accuracy; this anomaly is also present in similar graphs to follow.

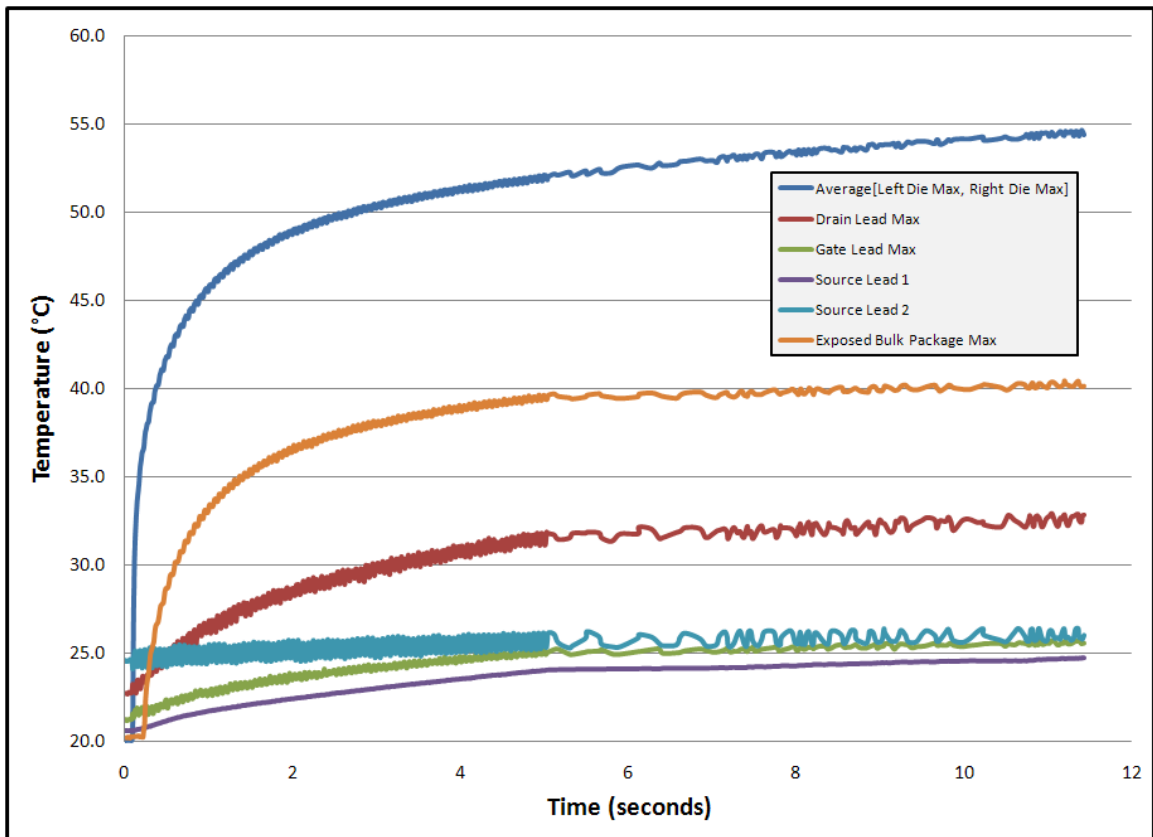


Figure 6.13 – Measured temperatures of the device die and clamping mechanism.

Of particular note are the temperatures of the MOSFET dice. The particular part has a maximum operational junction temperature of 200 °C, and the measured

temperature is asymptotically approaching 55 °C; additional data sets not included show that the maximum die temperature under steady state conditions is 55.7 °C. The very large amount of design margin in these parts will yield a significant increase in overall system reliability.

Figure 6.14 shows frame captures from the thermal camera, and illustrates how the temperatures in the system increase with respect to time. For the first 100 ms, only the dice are showing higher temperatures; beginning at the 200 ms mark, the rest of the package heats up, as does the clamping mechanism. The clamping mechanism does not experience surface temperatures above 33 °C, which is on the underside of the beam exerting force on the drain lead. The majority of the clamping mechanism does not rise above 24 °C, and the temperatures at the areas of highest structural stress, the region where the deflecting tabs meet the bulk of the clamping mechanism frame, do not exceed 22 °C. Ultem 2300 has a recommended maximum operating temperature of 171 °C and a glass transition temperature of 210 °C. Like the VHF MOSFET, the clamp is being operated at temperatures which are considerably lower than the material limit. This margin will ensure that any temperature accelerated degradation of the downforce will be minimal.

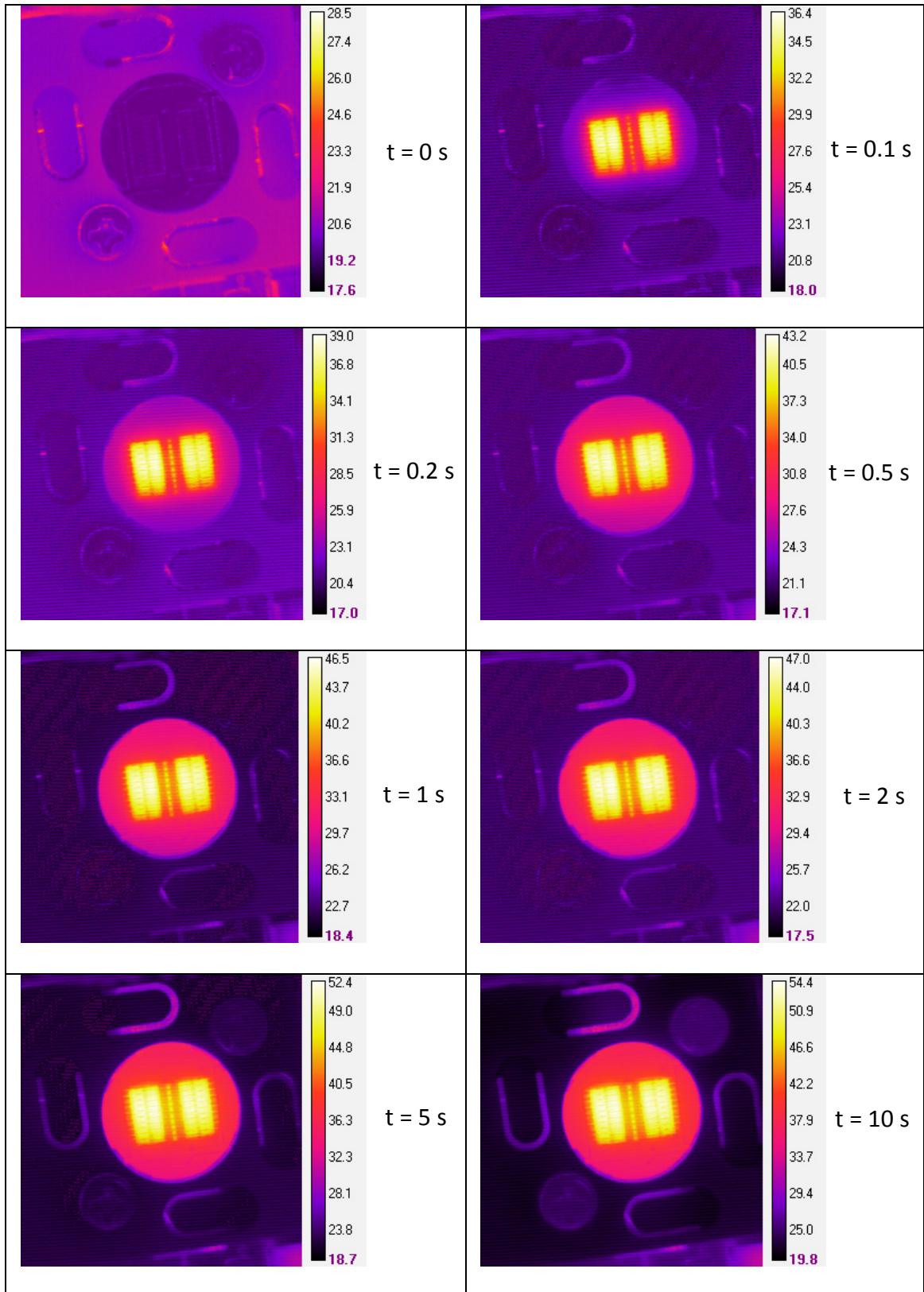


Figure 6.14 – Thermal images of the device die and clamping mechanism.

The temperature rate of change for the dice is plotted in Figure 6.15. Since the noise previously described has now been differentiated with respect to time, a pattern cannot be readily observed from the raw data. The data shown has been smoothed with the 'rloess' function in the Curve Fitting Toolbox of MATLAB R2009b, a modified local regression algorithm. The rate of change immediately after power is applied is above 600 °C/s, which is very high, but falls by an order of magnitude in approximately 50 ms. At approximately 800 ms, the rate of change has decreased by another order of magnitude to 6 °C/s, and by the three second mark, the rate of change has slowed to 1 °C/s.

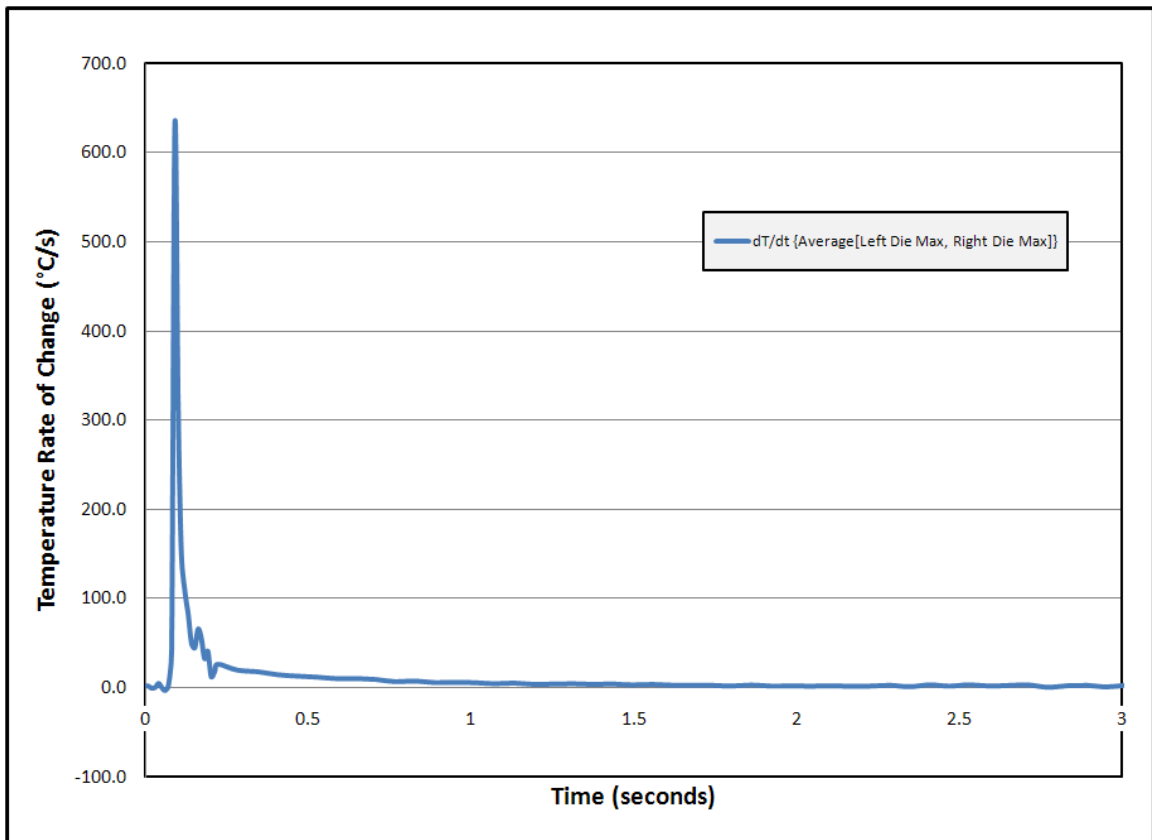


Figure 6.15 – Temperature rate of change of VHF MOSFET dice.

The temperature rate of change for the VHF MOSFET leads and the exposed bulk package is shown in Figure 6.16. This data has also been smoothed with the MATLAB 'rloess' function. The drain and gate lead, along with one source lead, heat up as power is applied, with the bulk of the package following approximately 130 ms later. The second source lead experiences very little heating, which is most likely due to an additional cooling path in the PCB. The rate of change for the bulk of the package decreases at a slower rate, which is to be expected due to the physical proximity to the dice.

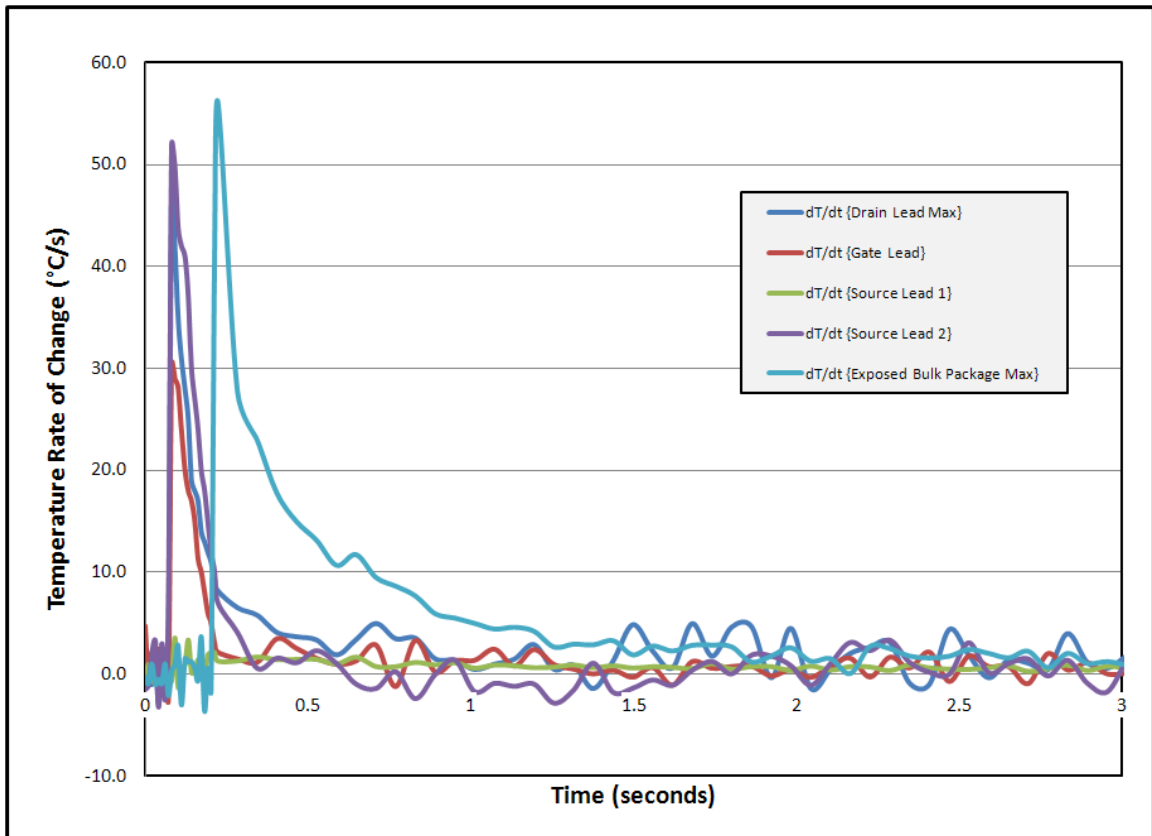


Figure 6.16 – Temperature rate of change of MOSFET leads and exposed bulk package.

Referring to Figure 6.15 and Figure 6.16, evidence of the different thermal time constants is easily discernible. The die reaches its τ_t value in about 15 ms, the drain, gate, and source leads in 80 ms, and the exposed bulk package in 240 ms. The longer time decay shown by the bulk package is due to its closer physical proximity to the brass MOSFET body, which has a theoretical τ_t of almost one second, as noted in Section 2.9. The rapid cooling rate of the die is possibly a combination of the high thermal diffusivity of the beryllium oxide and copper-molybdenum-copper and the large thermal mass of brass, which acts like a reservoir for the lower temperature of the heat sink, and from which the die can rapidly dissipate energy into.

CHAPTER 7 - CONCLUSIONS AND FUTURE WORK

The requirements and constraints of a clamped electrical connection have been presented. Theory and discussion regarding the forming of a connector out of two surfaces which were clamped together was supplemented with lab work and calculations showing that wear and abrasion were valid concerns for the system under analysis. Materials sufficient for the task were reviewed and four concepts were developed. Two of these concepts were prototyped and tested, one of which exhibited superior performance. The preferred clamping system was made out of a single injection molded piece of 30% glass filled polyetherimide, which can be expected to meet its stated requirements for multiple years.

Future efforts to expand on this topic could be in multiple areas. One obvious effort would be to fabricate more samples of the PEI clamp, with the aim of studying variability from part to part or between production batches. This would serve to demonstrate process repeatability and ensure that in full production, a very small percentage of the parts produced would not meet the system requirements.

Models for polymer relaxation exist, including those for long term aging of PEI, but detailed models which accurately represent the end usage environment are not readily available. Such models could be developed by performing elevated temperature testing similar to that detailed in Chapter 6, but with more samples and at a wider range

of temperatures. Efforts in this area would be beneficial in predicting with higher statistical confidence the relaxation behavior of the PEI clamp.

Alternate materials could be examined to determine if longer expected lifetimes are achievable in the form factor of the single piece molded clamp. Exotic and more costly materials such as polyether ether ketone offer potential performance improvements which were not pursued. Woven fabric reinforced composites such as those using carbon fiber or and woven fiberglass as the fabric and PEI or epoxy as the matrix were categorically excluded from this work but have been shown to provide impressive performance in cantilevered beam applications.

Diverging from the goal of increasing performance, effort could be spent attempting to reduce the cost as much as possible. If the constraints of radio frequency compatibility and expected usage of ten years are relaxed, inexpensive materials such as aliphatic polyamides (trademarked as Nylon by DuPont) or polycarbonate (trademarked as Lexan by SABIC) may prove to be sufficient. Less costly metals such as tempered steel may also be appropriate for lower frequency applications.

If significant resources were available, the clamping mechanism could theoretically be integrated into the device package. This type of design would require extensive collaboration with the semiconductor die manufacturer, but the potential cost reduction and manufacturability gains would be worthwhile for sufficiently high production volumes.

Regarding the thermal analyses and performance, better correlation between the theoretical and experimental values would be useful. More accurate data could

potentially be used to ensure that the VHF MOSFET was being operated with sufficient margin in more complex situations, such as a pulsed RF, modulated RF, or variable frequency RF application, which are commonplace in the semiconductor fabrication industry. Ideally, CAD packages such as FLUENT would be used to conceive and refine these models, and multiple trials of experimental data run to ensure statistical confidence.

REFERENCES

- [1] European Parliament and the Council of the European Union, "RoHS Compliance - Directive 2002/95/EC," 27-Jan-2003. [Online]. Available: <http://www.rohs.eu/English/Legislation/Docs/Launchers/Launch-2002-95-EC.html>. [Accessed: 30-Mar-2011].
- [2] S. Zangl and K. Moch, "Adaptation to Scientific and Technical Progress Under Directive 2002/95/EC - Evaluation of New Requests for Exemptions and/or Review of Existing Exemptions." Öko-Institut E.V. - Institute For Applied Ecology, Germany, 05-Aug-2010.
- [3] H. Ma and J. Suhling, "A Review of Mechanical Properties of Lead-Free Solders for Electronic Packaging," *Journal of Materials Science*, Vol. 44, No. 5, pp. 1141-1158, Mar. 2009.
- [4] M. Osterman and A. Dasgupta, "Life Expectancies of Pb-Free SAC Solder Interconnects in Electronic Hardware," *Journal Of Materials Science: Materials In Electronics*, Vol. 18, No. 1-3, pp. 229-236, Sep. 2006.
- [5] H. Ma, J. C. Suhling, Y. Zhang, P. Lall, and M. J. Bozack, "The Influence of Elevated Temperature Aging on Reliability of Lead Free Solder Joints," in *Electronic Components and Technology Conference, 2007. ECTC '07. Proceedings. 57th*, 2007, pp. 653-668.
- [6] Y. Zhang, Z. Cai, J. C. Suhling, P. Lall, and M. J. Bozack, "The Effects of Aging Temperature on SAC Solder Joint Material Behavior and Reliability," in *Electronic Components and Technology Conference, 2008. ECTC 2008. 58th*, 2008, pp. 99-112.
- [7] O. Russkikh and J. Sandera, "Reliability of Lead Free Solder SAC 305 for Chip Components Depending on Various Factors," in *Electronics System-Integration Technology Conference, 2008. ESTC 2008. 2nd*, 2008, pp. 471-476.
- [8] V. Venkatadri, Liang Yin, Yan Xing, E. Cotts, K. Srihari, and P. Borgesen, "Accelerating the Effects of Aging on the Reliability of Lead Free Solder Joints in a Quantitative Fashion," in *Electronic Components and Technology Conference, 2009. ECTC 2009. 59th*, 2009, pp. 398-405.
- [9] P. Biocca and C. Rivas, "Case Study on the Validation of SAC305 and SnCu Based Solders in SMT, Wave, and Hand-Soldering at the Contract Assembler Level." ITW Kester, 2006.
- [10] D. M. Anderson, *Design for Manufacturability & Concurrent Engineering; How to Design for Low Cost, Design in High Quality, Design for Lean Manufacture, and Design Quickly for Fast Production*. CIM Press, 2010.

- [11] Institute for Printed Circuits, "IPC-A-610D, Acceptability of Electronic Assemblies." 2005.
- [12] N. Duan, J. Scheer, J. Bielen, and M. Van Kleef, "The Influence of Sn-Cu-Ni(Au) and Sn-Au Intermetallic Compounds on the Solder Joint Reliability of Flip Chips on Low Temperature Co-fired Ceramic Substrates," *Microelectronics Reliability*, Vol. 43, No. 8, pp. 1317-1327, Aug. 2003.
- [13] D. Chong, F. Che, J. Pang, K. Ng, J. Tan, and P. Low, "Drop Impact Reliability Testing for Lead-Free and Lead-Based Soldered IC Packages," *Microelectronics Reliability*, Vol. 46, No. 7, pp. 1160-1171, Jul. 2006.
- [14] M. Abteu and G. Selvaduray, "Lead-Free Solders in Microelectronics," *Materials Science & Engineering Reports*, Vol. 27, No. 5-6, pp. 95-141, Jun. 2000.
- [15] M. Spraul, W. Nuchter, A. Moller, B. Wunderle, and B. Michel, "Reliability of SnPb and Pb-free Flip-Chips Under Different Test Conditions," *Microelectronics Reliability*, Vol. 47, No. 2-3, pp. 252-258, Mar. 2007.
- [16] D. Shangguan, *Lead-Free Solder Interconnect Reliability*. ASM International, 2005.
- [17] T. Pyzdek and P. A. Keller, *The Six Sigma Handbook: A Complete Guide for Green Belts, Black Belts, and Managers At All Levels*. McGraw Hill Professional, 2009.
- [18] J. M. Juran and Frank M. Gryna, *Juran's Quality Control Handbook*, 4th Ed. McGraw Hill, 1988.
- [19] A. C. Metaxas and R. J. Meredith, *Industrial Microwave Heating*. IET, 1983.
- [20] ST Microelectronics, "SD2933: RF Power Transistors." 2004.
- [21] Microsemi Corporation, "VRF2933: RF Power Vertical MOSFET, Datasheet." 2006.
- [22] "Kovar Products." [Online]. Available: <http://www.hcrosscompany.com/metals/kovar.htm>. [Accessed: 15-Apr-2011].
- [23] M. Antler, "Contact Fretting of Electronic Connectors," 1999.
- [24] M. Braunovic, V. Konchits, and N. Myshkin, *Electrical Contacts, Fundamentals, Applications, And Technology*. CRC Press, 2007.
- [25] J. Greenwood and J. Williams, "Contact of Nominally Flat Surfaces," *Proceedings of the Royal Society of London Series A - Mathematical, Physical, and Engineering Sciences*, Vol. 295, No. 1442, pp. 300-&, 1966.
- [26] J. Song and D. Srolovitz, "Mechanism for Material Transfer in Asperity Contact," *Journal of Applied Physics*, Vol. 104, No. 12, Dec. 2008.
- [27] G. Ferguson, M. Chaudhury, G. Sigal, and G. Whitesides, "Contact Adhesion of Thin Gold Films on Elastomeric Supports - Cold Welding Under Ambient Conditions," *Science*, Vol. 253, No. 5021, pp. 776-778, Aug. 1991.
- [28] W. Zhang and N. Bay, "Cold Welding - Experimental Investigation of Surface Preparation Methods," *Welding Journal*, Vol. 76, No. 8, pp. 326-330, 1997.
- [29] W. Zhang and N. Bay, "Cold Welding - Theoretical Modeling of The Weld Formation," *Welding Journal*, Vol. 76, No. 10, pp. S417-S420, Oct. 1997.
- [30] J. Song and D. Srolovitz, "Molecular Dynamics Investigation of Patterning Via Cold Welding," *Journal of the Mechanics and Physics of Solids*, Vol. 57, No. 4, pp. 776-787, Apr. 2009.

- [31] L. Vitos, A. V. Ruban, H. L. Skriver, and J. Kollár, "The Surface Energy of Metals," *Surface Science*, Vol. 411, No. 1-2, pp. 186-202, Aug. 1998.
- [32] ASTM International, "ASTM G40-10B Standard Terminology Relating to Wear and Erosion." 2010.
- [33] J. F. Archard, "Contact and Rubbing of Flat Surfaces," *Journal of Applied Physics*, Vol. 24, No. 8, p. 981, 1953.
- [34] H. Hensch, *Semiconductor Contacts - An Approach to Ideas and Models*. Clarendon Press, 1989.
- [35] J. G. Simmons, "Generalised Formula for the Electric Tunnel Effect Between Similar Electrodes Separated by a Thin Insulating Film," *Journal of Applied Physics*, Vol. 34, No. 6, p. 1793, Jun. 1963.
- [36] K. Kim, L. Ye, and C. Yan, "Fracture Behavior of Polyetherimide (PEI) and Interlaminar Fracture of CF/PEI Laminates at Elevated Temperatures," *Polymer Composites*, Vol. 26, No. 1, pp. 20-28, Feb. 2005.
- [37] I. Echeverria, P. Su, S. Simon, and D. Plazek, "Physical Aging of Polyetherimide - Creep and DSC Measurements," *Journal of Polymer Science Part B - Polymer Physics*, Vol. 33, No. 17, pp. 2457-2468, Dec. 1995.
- [38] S. Simon, "Enthalpy Recovery of Poly(Etherimide): Experiment and Model Calculations Incorporating Thermal Gradients," *Macromolecules*, Vol. 30, No. 14, pp. 4056-4063, Jul. 1997.
- [39] S. Simon, D. Plazek, J. Sobieski, and E. McGregor, "Physical Aging of Polyetherimide: Volume Recovery and its Comparison to Creep and Enthalpy Measurements," *Journal of Polymer Science Part B - Polymer Physics*, Vol. 35, No. 6, pp. 929-936, Apr. 1997.
- [40] J. Belana et al., "Physical Aging Studies in Polyetherimide Ultem 1000," *Polymer International*, Vol. 46, No. 1, pp. 29-32, May. 1998.
- [41] K. Liang, G. Banhegyi, F. Karasz, and W. Macknight, "Thermal, Dielectric, and Mechanical Relaxation in Poly(Benzimidazole) Poly(Etherimide) Blends," *Journal of Polymer Science Part B - Polymer Physics*, Vol. 29, No. 6, pp. 649-657, May. 1991.
- [42] F. Biddlestone, A. Goodwin, J. Hay, and G. Mouledous, "The Relaxation Spectrum and Physical Aging of Polyetherimide," *Polymer*, Vol. 32, No. 17, pp. 3119-3125, 1991.
- [43] E. Woo and S. Kuo, "A Nonlinear Regression Approach to Model the Physical Aging of Poly(Etherimide)," *Polymer Engineering And Science*, Vol. 37, No. 1, pp. 173-177, Jan. 1997.
- [44] L. Chacon, A. Arguelles, I. Vina, M. Castrillo, and J. Vina, "Study of the Behaviour of Glass-Fibre Fabric Reinforced PEI Subjected to Thermal Loads. Influence of Aging," *Advanced Composites Letters*, Vol. 16, No. 4, pp. 149-155, 2007.
- [45] J. Lincoln, R. Morgan, and E. Shin, "Effect of Thermal History on the Deformation and Failure of Polyimides," *Journal of Polymer Science Part B - Polymer Physics*, Vol. 39, No. 23, pp. 2947-2959, Dec. 2001.

- [46] J. Vina, M. Castrillo, A. Arguelles, and I. Vina, "A Comparison Between the Static and Fatigue Properties of Glass-Fiber and Carbon-Fiber Reinforced Polyetherimide Composites After Prolonged Aging," *Polymer Composites*, Vol. 23, No. 4, pp. 619-623, Aug. 2002.
- [47] R. P. Jewett, "Hydrogen Environment Embrittlement of Metals. NASA CR-2163." National Aeronautics and Space Administration, 1973.
- [48] "Hydrogen and Embrittlement." [Online]. Available: <http://www.sandia.gov/hydrogen/research/safetycodesstandards/hydrogenembrittlement.html>. [Accessed: 15-Jun-2011].
- [49] G. Tiwari et al., "A Study of Internal Hydrogen Embrittlement of Steels," *Materials Science and Engineering A - Structural Materials Properties*, Vol. 286, No. 2, pp. 269-281, Jul. 2000.
- [50] S. Chou and W. Tsai, "Effect of Grain Size on the Hydrogen-Assisted Cracking in Duplex Stainless Steels," *Materials Science and Engineering A - Structural Materials Properties*, Vol. 270, No. 2, pp. 219-224, Sep. 1999.
- [51] K. Sadananda and A. Vasudevan, "Fatigue Crack Growth Mechanisms in Steels," *International Journal of Fatigue*, Vol. 25, No. 9-11, pp. 899-914, Nov. 2003.
- [52] K. Cheong, K. Stevens, Y. Suzuki, and A. Takeuchi, "Investigating Creep Behaviour in Austenitic Stainless Steels Through Synchrotron X-Ray Tomography," *Advances in Heterogeneous Material Mechanics 2008*, pp. 1146-1149, 2008.
- [53] M. Amiri and M. Khonsari, "Life Prediction of Metals Undergoing Fatigue Load Based on Temperature Evolution," *Materials Science and Engineering A - Structural Materials Properties*, Vol. 527, No. 6, pp. 1555-1559, Mar. 2010.
- [54] A. Nagesha et al., "Thermomechanical Fatigue Evaluation and Life Prediction of 316L(N) Stainless Steel," *International Journal of Fatigue*, Vol. 31, No. 4, pp. 636-643, Apr. 2009.
- [55] T. Mayama and K. Sasaki, "Investigation of Subsequent Viscoplastic Deformation of Austenitic Stainless Steel Subjected to Cyclic Preloading," *International Journal of Plasticity*, Vol. 22, No. 2, pp. 374-390, 2006.
- [56] H. Murray, I. Zatz, and J. Ratka, "Fracture Testing and Performance of Beryllium Copper Alloy - C17510," 1994, Vol. 1184, pp. 109-133.
- [57] H. Burghardt and B. Weiss, "Fatigue Strength of a Copper Beryllium Alloy in Various Aging Conditions as a Function of Test Frequency and Loading Mode," *Zeitschrift Fur Metallkunde*, Vol. 66, No. 11, pp. 681-685, 1975.
- [58] L. P. Pook, "Effect of Hardness and Tensile Mean Stress on Fatigue Crack Growth in Beryllium Copper," *Journal of Mechanical Engineering Science*, Vol. 11, No. 3, pp. 343-350, 1969.
- [59] R. Bagheri and G. Miller, "Fatigue and Corrosion Fatigue of Beryllium-Copper Spring Materials," *Journal of Testing and Evaluation*, Vol. 21, No. 2, pp. 101-106, Mar. 1993.
- [60] E. Staniek, R. Seguela, B. Escaig, and P. Francois, "Plastic Behavior of Monoclinic Polypropylene Under Hydrostatic Pressure in Compressive Testing," *Journal of Applied Polymer Science*, vol. 72, no. 10, pp. 1241-1247, Jun. 1999.

- [61] M. Celina, K. Gillen, and R. Assink, "Accelerated Aging and Lifetime Prediction: Review of Non-Arrhenius Behaviour Due to Two Competing Processes," *Polymer Degradation and Stability*, Vol. 90, No. 3, pp. 395-404, Dec. 2005.
- [62] K. Gillen, R. Bernstein, and M. Wilson, "Predicting and Confirming the Lifetime of O-Rings," *Polymer Degradation and Stability*, Vol. 87, No. 2, pp. 257-270, Feb. 2005.
- [63] K. Gillen, M. Celina, and R. Bernstein, "Validation of Improved Methods for Predicting Long-Term Elastomeric Seal Lifetimes from Compression Stress-Relaxation and Oxygen Consumption Techniques," *Polymer Degradation and Stability*, Vol. 82, No. 1, pp. 25-35, Oct. 2003.
- [64] R. Bernstein, D. Derzon, and K. Gillen, "Nylon 6.6 Accelerated Aging Studies: Thermal-Oxidative Degradation and its Interaction with Hydrolysis," *Polymer Degradation and Stability*, Vol. 88, No. 3, pp. 480-488, Jun. 2005.
- [65] R. Bernstein and K. Gillen, "Predicting the Lifetime of Fluorosilicone O-Rings," *Polymer Degradation and Stability*, Vol. 94, No. 12, pp. 2107-2113, Dec. 2009.
- [66] R. Bernstein and K. Gillen, "Nylon 6.6 Accelerating Aging Studies II: Long-Term Thermal-Oxidative and Hydrolysis Results," *Polymer Degradation and Stability*, Vol. 95, No. 9, pp. 1471-1479, Sep. 2010.
- [67] K. Gillen, M. Celina, R. Clough, and J. Wise, "Extrapolation of Accelerated Aging Data - Arrhenius or Erroneous?," *Trends in Polymer Science*, Vol. 5, No. 8, pp. 250-257, Aug. 1997.
- [68] H. W. McLean, *HALT, HASS, and HASA Explained: Accelerated Reliability Techniques*. ASQ Quality Press, 2000.